Trabajo Fin de Grado
Grado en Ingeniería Aeroespacial

Numerical Analysis for Dynamic Stall Control Elements on Vertical-Axis Wind Turbines

Autor: Miguel Cuesto Rubio

Tutor: Luis Balam Modesto López

Dpto. Ingeniería Aeroespacial y Mecánica de Fluidos
Escuela Técnica Superior de Ingeniería
Universidad de Sevilla

Sevilla, 2019

Trabajo Fin de Grado
Grado en Ingeniería Aeroespacial

Numerical Analysis for Dynamic Stall Control Elements on Vertical-Axis Wind Turbines

Autor:
Miguel Cuesto Rubio

Tutor:
Luis Balam Modesto López
Profesor Contratado Doctor

Dpto. Ingeniería Aeroespacial y Mecánica de Fluidos
Escuela Técnica Superior de Ingeniería
Universidad de Sevilla

Sevilla, 2019

Trabajo Fin de Grado: Numerical Analysis for Dynamic Stall Control Elements on Vertical-Axis Wind Turbines

Autor: Miguel Cuesto Rubio
Tutor: Luis Balam Modesto López

El tribunal nombrado para juzgar el trabajo arriba indicado, compuesto por los siguientes profesores:

Presidente:

Vocal/es:

Secretario:

acuerdan otorgarle la calificación de:

El Secretario del Tribunal

Fecha:

Agradecimientos

Este trabajo fin de grado marca el final de una etapa comenzada hace 4 años, una etapa marcada por penas y glorias, pero de la que realizo un balance general muy positivo. Por supuesto, esto no habría sido posible sin la inestimable ayuda de mis padres, de mi hermana, y de mis amigos, de Sevilla, de Huelva, y de todas las partes del mundo. ¡El futuro es verde!

Resumen

La energía eólica está demostrando ser un medio de generación de energía cada vez más fiable y eficiente, al ser posible una generación de energía en masa y libre de subsidios económicos. Esto está todo siendo conseguido por las turbinas eólicas de eje horizontal (HAWTs). Sin embargo, existe otro tipo de turbinas de eje vertical (VAWTs), que tras una pausa de una década, están volviendo a ser investigadas.

Las VAWTs podrían posibilitar generación de energía silenciosa y eficiente en ambientes urbanos o muy cambiantes, donde la naturaleza inflexible de las HAWTs (por ejemplo, las HAWTs no pueden adaptarse a cambios grandes en la dirección del viento) las limita. Uno de los principales problemas a los que se enfrenta la implementación de VAWTs es la ocurrencia de entrada en pérdida dinámica a ciertos ángulos relativos a la dirección del viento. La entrada en pérdida afecta gravemente a la turbina, decreciendo el par dinámico y por tanto la energía generada, además de creando momentos flectores que pueden afectar la estructura de la turbina en general.

Por tanto, el objetivo de este proyecto es estudiar la posibilidad de evitar la entrada en pérdida implementando en la pala elementos pasivos simples de control, y determinar el efecto de estos elementos pasivos en la generación de energía, comparado con el caso de turbina base. Al contrario de los dispositivos activos de control (por ejemplo, ”jets” sintéticos o control de cabeceo), los elementos pasivos tienen como objetivo la simplicidad estructural, lo que es un requisito para las aplicaciones domésticas. De esta manera, es posible ofrecer costes bajos de adquisición y mantenimiento.

Abstract

Wind energy is proving to be an increasingly more reliable, efficient means of generating energy, as mass, subsidy-free power generation becomes a reality. This is all being achieved by Horizontal-Axis Wind Turbines (HAWTs). Nonetheless, there is also another type of turbines, namely Vertical-Axis Wind Turbines (VAWTs), which after a decade-long hiatus, are being widely researched again.

VAWTs could enable efficient, quiet power generation in urban or highly-changing environment, where the inflexible nature of HAWTs (for example, HAWTs cannot adapt to large wind heading changes) is limiting. One of the main problems faced by the implementation of VAWTs is the occurrence of dynamic stall at certain angles relative to the wind heading. Stall affects the turbine severely, decreasing torque and therefore power generation as well, and creating bending moments which can affect the structure of the overall turbine.

Thus, the objective of this project is to study the avoidance of dynamic stall by implementing simple passive stall control devices on the blade, and determine their effect on power generation when compared to the clean turbine. As opposed to active stall control devices (for example, synthetic jets or pitch control), passive devices aim for structural simplicity, which is demanded for domestic application, so as to offer low upfront and maintenance costs.

Contents

1 Introduction

1.1 Current Status of Wind Energy in Europe

Wind energy has enjoyed steady growth in terms of installed capacity around the world since the 1990s. As per the association for wind energy in Europe (Wind Europe, previously EWEA [1]), the installed capacity in the continent has increased exponentially in a mere 10 years. As an example, this number was 12.8 GW back in 2000 and already increased tenfold to 192 GW by 2015. Such an evolution is illustrated in Figure 1.1.

As a goal for the future, Europe shall have an installed capacity of 323 GW by 2030, divided in mass onshore (253 GW), offshore (70GW) and purely domestic applications.

Offshore applications have seen a strong increase in the last decade as primarily western European countries have decided on significant projects in the North Sea. For instance, this has enabled Denmark and Ireland to rely strongly on wind energy for national energy production, namely 37% for the former and 27% for the latter. Globally, the percentage of wind energy in the EU energy mix amounts to 11%.

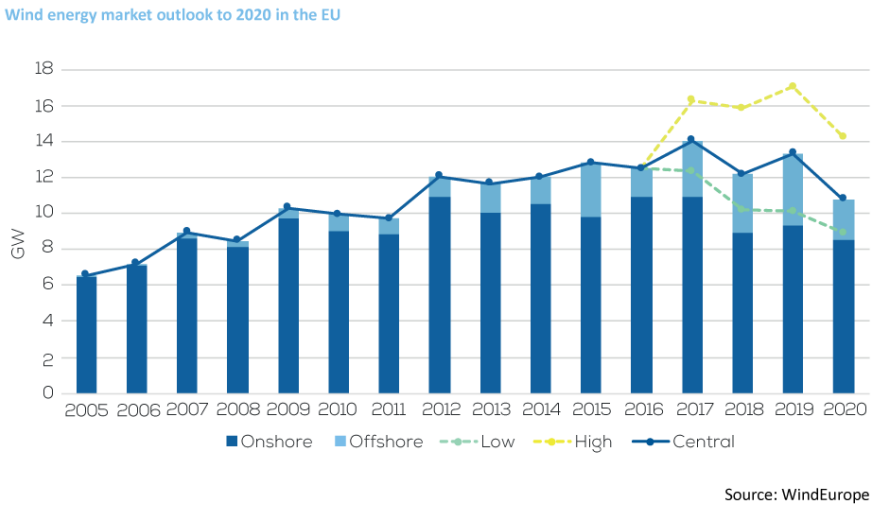

Figure 1.1 Evolution of yearly wind energy capacity installation.

Analysing the market in Spain, the nation's wind installed capacity adds up to 23 GW, that number enabling Spain to be the 5th largest wind-producing country, after China, the US, Germany and India [2]. Inside the domestic market, wind energy was the second most important energy source for electricity generation in 2017, after nuclear power, producing 20% of all electrical power in the country. Nonetheless, this infrastructure is overwhelmingly an onshore application, as offshore wind farms are still experimental at a national level, even though there is measurable wind resource available to be exploited, especially around Andalusian coastal areas [3].

1.2 Developments on urban Wind Energy

In the last 20 years, focus in research has been shifted to wind energy production in urban environments. As per [4], three modes of integration in buildings have been mainly pursued as follows:

- integration of traditional free-standing wind turbines in buildings.
- retrofit of wind turbines onto already existing buildings.
- integration of specifically-designed wind turbines for urban implementation purposes.

Such wind turbines are the object of this study, the so-called vertical-axis wind turbines (VAWTs from now on). In contrast to horizontal-axis models (HAWTs), VAWTs do not need to yaw to adjust to wind direction, as energy production is independent of this factor. Moreover, their lower rotational speeds (and overall smaller sizes) hinder a noise pollution problem. As an example, in rooftop applications, the noise level produced by the turbines themselves is normally lower than the one produced by wind shear as the current tries to shape its way past the building [5].

1.3 VAWT typology

VAWTs can be divided into 3 main types: Savonius, Darrieus and hybrid wind turbines, as seen on Figure 1.2.

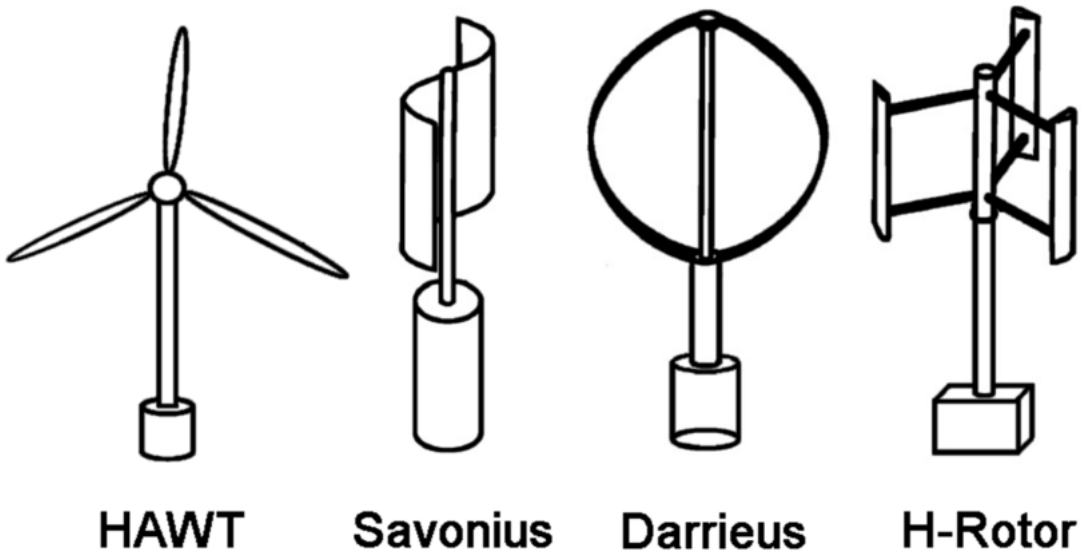

Figure 1.2 Savonius, Egg beater (type 1 Darrieus), and H-rotor (type 2 Darrieus) turbines, compared to a HAWT [6].

1.3.1 Savonius turbines

Savonius wind turbines are based on drag forces which makes them spin, due to their specific shaping. This very shaping also implies a lower flow energy utilisation in contrast to Darrieus wind turbines, and thus a comparatively lower efficiency [7]. The main advantage to this type is its self-starting ability, due to good starting torques when compared to lift-based models.

1.3.2 Darrieus turbines

These turbines feature high efficiencies but no self-starting abilities, as they are lift-based. However, their lift generation mechanisms can place a great level of strain on the blades and tower, even reaching breaking points for certain materials. One can classify Darrieus turbines in two larger groups.

- Egg beater-shaped Darrieus VAWTs feature two curved blades which meet at a lower and upper hub at the tower. The geometry enables minimal bending moment on the blades, thus enabling larger wind turbines following this principle, and hence getting into megawatt-producing areas as well. This being said, this complex geometry also implies limited mass production and higher costs.

- Straight-bladed wind turbines (also called H-rotors) are most often built up of two or three blades with constant airfoil features and rotating around a hub with a constant radius. **Production costs** are comparatively lower, while the experienced **bending moments** are highest. Said structural issues though don't pose a problem in the kilowatt operational area, such as for urban, **domestic applications**, while severely limiting their prospects as a mass energy production medium. Furthermore, the **blade geometry** associated to H-rotors can induce problems associated with unsteady aerodynamics, which can decrease the energy yield strongly.

The object of this project is thus to answer the question **"Is there a way to improve Straight-bladed VAWT performance, by means of mitigating the effects produced by dynamic stall?"**.

1.3.3 Hybrid turbines

Self-starting capabilities at low wind velocity are incorporated into a Darrieus turbine, this being enabled by an additional Savonius rotor in the setup.

2 Physical Background

2.1 The double-multiple Streamtube Theory (DMS)

I. Paraschivoiu undertook in 1988 an analysis of Darrieus rotor aerodynamics through the double-multiple streamtube theory [8], taking the Blade Element Momentum (BEM) method as its base. In the former, each section of the overall rotor is made up of a pair of actuator disks in tandem (conversely, only one actuator disk is used for BEM). Henceforth, the study on the induced velocities is undertaken separately in the up- and downstream halves, and each half is further divided in multiple aerodynamically independent streamtubes. This means, the streamtubes are supposed not to interact with each other. A schematic view on the streamtubes and their induced velocities is as per Figure 2.1.

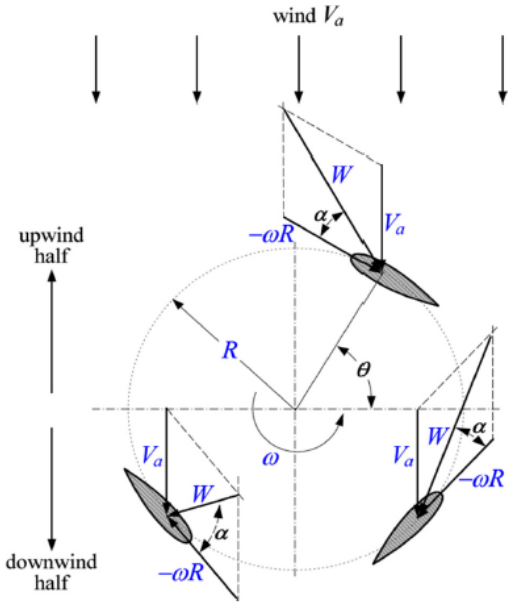

Figure 2.1 Relative velocity diagram on the level of a Darrieus turbine [9].

2.1.1 Upwind kinematic analysis

The upwind velocity (V) is less than the local ambient air velocity ($V_{\infty 1}$), them being related through an interference factor u, less than 1:

$$V' = uV_{\infty 1} \tag{2.1}$$

Additionally, the equilibrium velocity in the plane between both upstream and downstream currents (V_e) is also less than V:

$$V_e = (2u - 1)V_{\infty 1} \tag{2.2}$$

Therefore, the induced velocity (V') decreases in the axial streamtube direction, so V' $< V_e$. The upwind, induced and rotational velocities form a velocity triangle, which can be seen on Figure 2.1. For -$\pi/2 \leq \theta \leq \pi/2$, the local velocity of the upstream is given by:

$$Wu = \sqrt{Vu^2[(\lambda - \sin\theta)^2 + \cos^2\theta]} \tag{2.3}$$

With λ being the so-called local tip speed ratio (TSR), which links local blade speeds and air speeds:

$$\lambda = \frac{\omega R}{V'} \tag{2.4}$$

The local angle of attack (α) is defined as follows:

$$\alpha = arcsin\left(\frac{cos\theta cos\alpha_0 - (X - sin\theta)sin\alpha_0}{\sqrt{[(\lambda - sin^2\theta)^2 + cos^2\theta]}}\right) \tag{2.5}$$

In this case, α_0 is the residual pitch of the blade, alas, the angle between the tangent line pertaining to the rotation circumference and the blade chord. Furthermore, a local Reynolds number can be defined, which measures the viscous behaviour of the air:

$$Re = \frac{\rho Wuc}{\mu}, \tag{2.6}$$

where $\rho$is the density, Wu the local velocity, c the chord of the airfoil and $\mu$the dynamic viscosity of the air.

2.1.2 Dynamic analysis

Akin to lift and drag forces, we can define the tangential and normal forces on the turbine blade:

$$F_N(\theta) = \frac{1}{2}\rho cLW^2 C_N \tag{2.7}$$

$$F_T(\theta) = \frac{1}{2}\rho cLW^2 C_T \tag{2.8}$$

In the latter expressions, ρ is the density of the fluid, c the blade chord, L its length (can also be interpreted as H, blade height), and C_N and C_T are the non-dimensional coefficients of the normal and tangential forces, respectively.

$$C_N = C_L cos\alpha + C_D sin\alpha \tag{2.9}$$

$$C_T = C_L sin\alpha - C_D cos\alpha \tag{2.10}$$

C_L and C_D are the so-called lift and drag coefficients, respectively. They are obtained as dimensionless coefficients which characterise the lift and drag forces acting upon an airfoil. Their distribution on an airfoil with respect to the inflow velocity is illustrated by Figure 2.2.
The lift coefficient is:

$$C_L = \frac{L}{\frac{1}{2}\rho V^2 S}, \tag{2.11}$$

And the drag coefficient:

$$C_D = \frac{D}{\frac{1}{2}\rho V^2 S}, \tag{2.12}$$

V in this case being the relative velocity between airfoil and inflow.

The torque produced locally is calculated as per the following (R being the turbine radius, from the turbine tower to the rotation circumference):

$$Q(\theta) = F_T(\theta)R \tag{2.13}$$

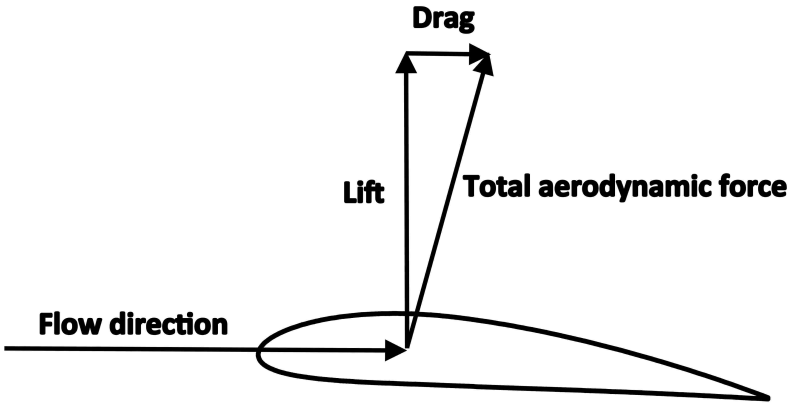

Figure 2.2 Aerodynamic forces on an airfoil [10].

And ultimately, the torque provided by the upstream half is as per:

$$Q_u = \frac{N}{2\pi}\int_{-\pi/2}^{\pi/2} \mathrm{Q}(\theta)\,\mathrm{d}\theta \tag{2.14}$$

A non-dimensionalisation further provides C_{Q_u}:

$$C_{Q_u} = \frac{Q_u}{\frac{1}{2}\rho V'^2 SR} \tag{2.15}$$

2.1.3 Power analysis

The power coefficient for the upstream half is calculated through:

$$C_{P_u} = C_{Q_u}\lambda_r \tag{2.16}$$

In this case, λ_r is the rotor TSR, defined through $\lambda_r = R\omega/V_{\infty 1}$. Following the same procedure for the downstream half (for $\pi/2 \leq \theta \leq 3\pi/2$), C_{P_d} shall be obtained, and thus, the total power coefficient shall be $C_P = C_{P_u} + C_{P_d}$. As an additional remark, the DMS theory does not assume unsteady flow and thus there is no consideration for phenomena such as **dynamic stall**.

2.2 Dynamic Stall

Stall is a phenomenon which occurs when the angle of attack perceived by the airfoil increases past the angle at which the lift coefficient is maximum ($C_{L_{max}}$). As can be seen on Figure 2.3, C_L behaves linearly until $C_{L_{max}}$, when the coefficient reaches a plateau and then plummets. This decrease is produced by a separation of the current away from the airfoil.

A VAWT blade is constantly rotating at a speed ω, and therefore the perceived angle of attack by the blade is also constantly changing, under the assumption that the wind direction remains constant. This perceived angle of attack nonetheless changes with the turbine TSR, as per the formula in section 2.1. This is shown on Figure 2.4, which illustrates the perceived angles of attack for $\lambda = 2,3,4,5$. Taking $\alpha_{C_{L_{max}}} \approx 13$ as an example, it can be determined that the turbine will experience stall for $\lambda < 4$.

This constant change of angle of attack along the azimuth position induces large contrasts in lift and drag forces in the turbine operational area. It is so, that for certain instants the turbine may experience deceleration, as for high angles of attack drag forces will prevail. This disparity along the azimuth also puts a sizeable structural strain on the tower and the turbine overall, as certain blades might be stalled and others might not at any given point. Vibratory loads are just as important under dynamic stall conditions, leading to structural fatigue and noise.

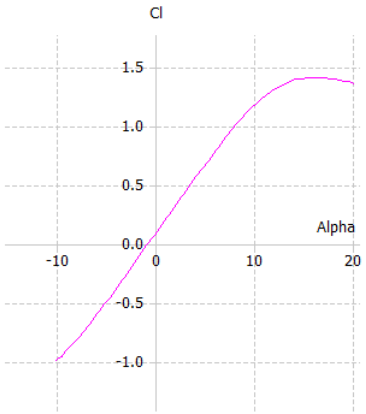

Figure 2.3 C_L against α for a DU 06-W-200 airfoil.

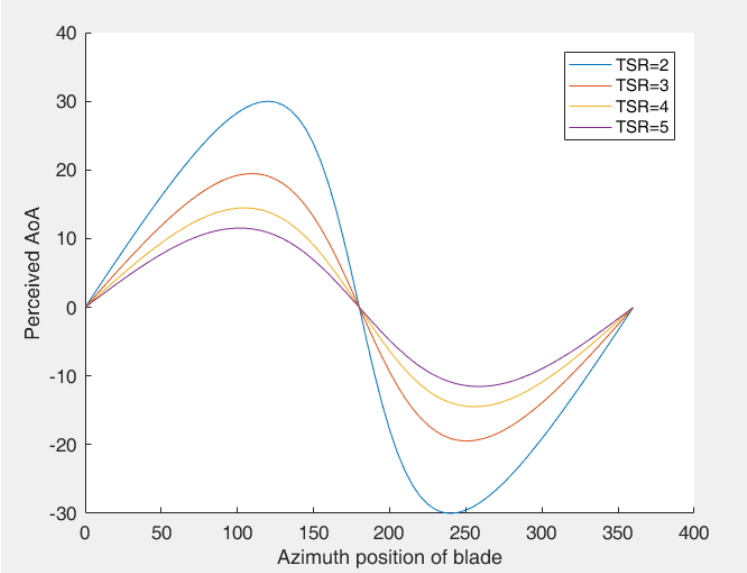

Figure 2.4 α against θ for a VAWT airfoil.

Under dynamic stall, the turbine experiences shed vorticity, VAWTs being especially sensitive to such phenomenon. A vortex created and shedded on the upstream passage of the blade may affect the blade further on the downstream half. This vortex induces an unfavourable current situation on the blade, even thought it may not be under stall conditions due to its azimuth position.

2.3 The Lifting Line Theory (LLT)

The double-multiple streamtube method is nevertheless just valid as a first approximation, as convergence problems arise in case of high blade loading, high solidities or high TSRs. Therefore, for further preliminary study the LLT can be used, as such convergence problems lessen, and computational costs are lower than those usual for RANS- or LES-based Computational Fluid Dynamics (CFD) simulations. This method was developed by Marten et al. [11], and incorporated into their open-source turbine design software suite, QBlade, which will be used in this study.

It is worth noting that for VAWTs there is still no certification-grade software which is low on computational cost, like GH Bladed for HAWTs. That is why for model verification, CFD has to be used and ultimately wind tunnel experiments should also be undertaken.

2.3.1 Physical fundamentals

For each time step, blade forces are calculated using the 1/4-chord line as the lifting line, which contains distributed vortices (hence the overall circulation in the blade being Γ_l, calculated through tabulated specific parameters for the airfoil, as well as the inflow angle for the timestep). Downstream from the airfoil, the wake is calculated through free-flowing vortex elements which separate from the trailing edge of the airfoil. For the case of HAWTs, wake vortex elements can be said to have a negligible influence after a certain downstream distance from the airfoil and are therefore truncated at a certain age. This is mainly due to the fact that for the wake of a HAWT, the trailing vorticity is dominant. Such an approximation cannot be made for a VAWT, as the angle of attack is changing constantly and therefore, trailing and shed vorticity effects are equally significant.

The strategy for VAWTs is therefore rather a reduction on the wake, as it can be assumed that for every time step, there are vortices separating from the trailing edge with negligible circulation. As an example, for straight-bladed turbines (the case which shall be further studied), shed vorticity is negligible at low blade loading positions, and trailing vorticity from inner blade sections [11]. Thus, reducing shed vorticity in the model enables this method to have a lower computation cost, as a 50% reduction on vorticity decreases the computation time by 75%, while it can be ensured that the difference is not any greater than 1%, in comparison to there not being any vortex reduction.

This method is nonetheless best suited for studies in high TSR cases, as there is no consideration for dynamic stall situations, and a successful calculation is dependent on good polar data. As an example, after setting up an airfoil, QBlade calculates the airfoil polar for a restricted azimuth through XFOIL and then extrapolates using the Viterna-Corrigan method for $0 \leq \theta \leq 2\pi$. This yields an unrealistic result for low TSRs when compared to an experimentally-obtained aircraft polar, which takes phenomena such as dynamic stall into account. This study was undertaken in [12]. Figure 2.5, also taken from the same study, shows the effect of dynamic stall on the power coefficient (in red), and subsequently the disparity with the stall-absent case (in blue).

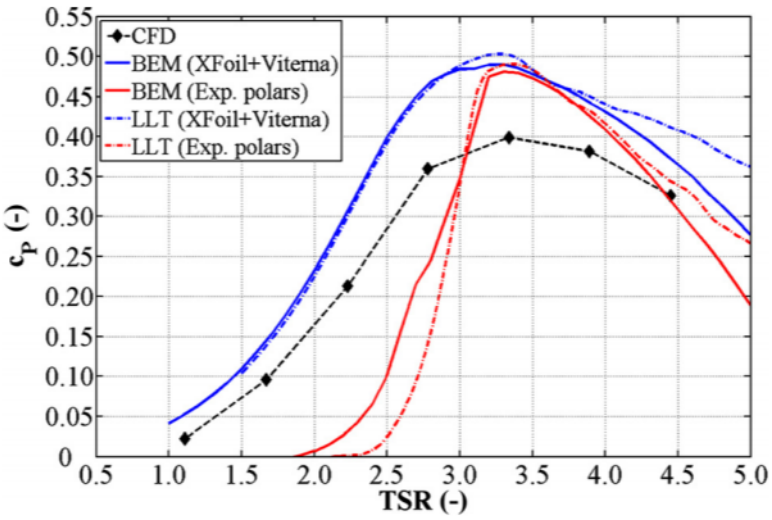

Figure 2.5 Influence of dynamic stall on the power coefficient.

2.4 Computational Fluid Dynamics (CFD)

ANSYS Fluent will be used as the CFD analysis tool for the project. CFD is needed for a potentially more exact turbine performance calculation, especially due to the built-in turbulence models. The reason is that turbulence follows highly chaotic and time-dependent behaviours which the forementioned, simplified methods fail to take into account.

2.4.1 Fundamentals of CFD

The main principle behind CFD is the discretisation of variables. Through this discretisation:

- Continuous variables are approximated into their values in a finite amount of points (these points being called nodes).
- Derivatives are therefore converted into algebraic differences.
- Equations which make use of discretised variables, work out values in the nodes. This means, the system of partial differential equations (PDEs, namely Reynolds-Averaged Navier-Stokes equations) associated with CFD will be applied to the given nodes.

Furthermore, there are several methods for discretising:

- Finite Difference Method (FDM): continuous variables are supposed to vary linearly between two given points, and therefore derivatives are calculated as slopes. As an example, $\frac{\partial x}{\partial y} \approx \frac{x_{i+1,j}-x_{i-1,j}}{2\Delta y}$.
- Finite Element Method (FEM): the nodes form a coarse grid, which in turn is composed by nodes being linked to their closest ones (each polygon being its own ”finite element”. This way, the PDEs can be solved simply for every finite element. Later on, these solutions are used to further assemble a system of equations which obtains the global solution of the given problem.
- Finite Volume Method (FVM): a finite volume is assembled around each node and the variables are supposed to make up a conservative flux (the input and output flows are the same). This way, volume integrals part of a PDE can be converted into surface integrals by the theorem of divergence. These newly-converted terms are then evaluated as fluxes at the surface of each finite volume. This is the method behind ANSYS Fluent and CFD.

After designing the geometry and the flow field, the flow field is discretised and a mesh is formed. The PDEs are then evaluated at the nodes, through which the PDEs are transformed into a system of algebraic equations. These equations are then solved numerically, thus obtaining values for every node in the mesh.

2.4.2 Reynolds-Averaged Navier-Stokes equations (RANS)

Assuming incompressible flow, the Continuity equation is:

$$\frac{\partial \rho}{\partial t} + \nabla \cdot (\rho u) = 0, \tag{2.17}$$

where ρ is the density of the fluid (constant due to incompressible flow), ∇ the nabla operator, and $u(x,t)$ the velocity. Similarly, the Momentum equation is:

$$\frac{\partial u}{\partial t} = u \cdot \nabla u - \nu \Delta u = -\frac{1}{\rho}\nabla p + g, \tag{2.18}$$

where ν is the kinematic viscosity ($\nu = \frac{\mu}{\rho}$), $p(x,t)$ is the pressure, and g are the volume forces which act upon the flow (i.e gravity). Averaging in time, the Continuity equation transforms into:

$$\nabla \cdot U = 0, \tag{2.19}$$

while the time-averaged Momentum equation is:

$$\frac{\partial U}{\partial t} + U \cdot \nabla U - \nu \Delta U = -\frac{1}{\rho}\nabla P + G - \frac{1}{\rho}(\overline{\rho u' \cdot \nabla u'}),. \tag{2.20}$$

where U, P, and G are the time-averaged components of the velocity, pressure and volume forces respectively, and u' is the fluctuating component of the velocity. These are the so-called Reynolds Averaged Navier-Stokes equations, also RANS equations.

2.4.3 Reynolds turbulence

As seen in the time-averaged Momentum function, velocity can be decomposed into an averaged component (U), and a fluctuating component (u'), thus being $u = U + u'$. The fluctuating component of velocity can

be traced back to turbulence, which is a 3D, transient, fluctuating movement associated to a time-averaged main flow.

The term $-\frac{1}{\rho}(\overline{\rho u' \cdot \nabla u'})$, also defines the turbulence in the time-averaged Momentum equation. In tensor notation, can be written as $\frac{\partial}{\partial x_j}(\overline{\rho u_i' u_j'})$. The expression between the brackets is the Reynolds tensor, $\tau_{ij} = \overline{\rho u_i' u_j'}$, where the first index indicates the plane of action of the stress, and the second index indicates the direction upon which the stress acts [13].

Reynolds stresses cannot be known beforehand for turbulent current cases, and therefore they need to be modelled. One method to model the Reynolds stresses is through eddy viscosity. The Boussinesq eddy viscosity approximation is as follows:

$$-\overline{\rho u_i' u_j'} = \nu_t(\frac{\partial U_i}{\partial x_j} + \frac{\partial U_j}{\partial x_i}) - \frac{2}{3}k\delta_{ij}, \tag{2.21}$$

where k is the turbulent kinetic energy and ν_t the eddy viscosity. Both variables are still unknown, but they can be modelled through several methods. In our research, they will have a common modelling equation for k, and a more sophisticated system of equations for ν_t.

2.4.4 The $k-$equation

It is sensible to begin the turbulence equation definition by shaping up a kinetic energy model, and thus modeling the characteristic velocity component of a turbulent field as the square root of the kinetic energy pertaining to the field:

$$k = \frac{1}{2}(\overline{u_x' u_x'} + \overline{u_y' u_y'} + \overline{u_z' u_z'}) \tag{2.22}$$

It can be seen that k equals the sum of the Reynolds stresses multiplied by 0.5. Thus, using the Reynolds stress equation (the calculation process goes beyond the scope of this study):

$$\rho\frac{\partial k}{\partial t} + \rho\frac{\partial}{\partial x_j}(U_j k) = \tau_{ij}\frac{\partial U_i}{\partial x_j} - \mu\overline{\frac{\partial u_i'}{\partial x_k'}\frac{\partial u_i'}{\partial x_k'}} + \frac{\partial}{\partial x_j}\left(\mu\frac{\partial k}{\partial x_j} - \frac{1}{2}\rho\overline{u_i' u_i' u_j'} - \overline{p' u_j'}\right) \tag{2.23}$$

The term $\mu\overline{\frac{\partial u_i'}{\partial x_k'}\frac{\partial u_i'}{\partial x_k'}}$ is of special interest for this study on fluid dynamics, as it represents the dissipation of kinetic energy in terms of heat, at a molecular level. This dissipation is denoted by ε:

$$\varepsilon = \nu\overline{\frac{\partial u_i'}{\partial x_k'}\frac{\partial u_i'}{\partial x_k'}} \tag{2.24}$$

As $\frac{\partial u_i'}{\partial x_k'}$ will always be positive, it can be determined that ε will imply a loss of energy away from the flow, by means of dissipation.

2.4.5 The $k-\varepsilon$ Turbulence Model

The $k-\varepsilon$ turbulence model adds two additional equations to the RANS. The $k-$equation:

$$\rho\frac{\partial k}{\partial t} + \rho U_j\frac{\partial k}{\partial x_j} = \frac{\partial}{\partial x_j}\left(\left[\mu + \frac{\mu_t}{\sigma_k}\right]\frac{\partial k}{\partial x_j}\right) + \tau_{ij}\frac{\partial U_i}{\partial x_j} - \rho\varepsilon, \tag{2.25}$$

and the ε-equation:

$$\rho\frac{\partial \varepsilon}{\partial t} + \rho U_j\frac{\partial \varepsilon}{\partial x_j} = \frac{\partial}{\partial x_j}\left(\left[\mu + \frac{\mu_t}{\sigma_\varepsilon}\right]\frac{\partial \varepsilon}{\partial x_j}\right) + C_{\varepsilon 1}\frac{\varepsilon}{k}\tau_{ij}\frac{\partial U_i}{\partial x_j} - C_{\varepsilon 2}\rho\frac{\varepsilon^2}{k} \tag{2.26}$$

The eddy viscosity μ_t is to be calculated through $\mu_t = \frac{\rho C_\mu k^2}{\varepsilon}$. $C_{\varepsilon 1}, C_{\varepsilon 1}, C_\mu$, σ_ε and σ_k are empirically obtained closure coefficients.

2.4.6 The $k-\omega$ Turbulence Model

The $k-\omega$ turbulence model defines a specific dissipation rate (ω). Thus, this model solves for the rate of destruction of turbulent kinetic energy, while the $k-\varepsilon$ model solves for the magnitude of this very destruction. As $\omega = c\frac{\sqrt{k}}{l}$, c being a constant. Therefore, ω is dimensionally equivalent to $\frac{\varepsilon}{k}$.

Two equations are also added to the RANS. The $k-$equation:

$$\rho\frac{\partial k}{\partial t}+\rho U_j\frac{\partial k}{\partial x_j}=\frac{\partial}{\partial x_j}\left(\left[\mu+\sigma_k\mu_t\right]\frac{\partial k}{\partial x_j}\right)+\tau_{ij}\frac{\partial U_i}{\partial x_j}-\beta^*\rho k\omega, \tag{2.27}$$

and the ω-equation:

$$\rho\frac{\partial \omega}{\partial t}+\rho U_j\frac{\partial \omega}{\partial x_j}=\frac{\partial}{\partial x_j}\left(\left[\mu+\mu_t\sigma_\omega\right]\frac{\partial \varepsilon}{\partial x_j}\right)+\alpha\frac{\omega}{k}\tau_{ij}\frac{\partial U_i}{\partial x_j}-\beta\rho\omega^2 \tag{2.28}$$

The eddy viscosity μ_t is to be calculated through $\mu_t=\frac{\rho k}{\omega}$. α, β, β^*, σ_ω and σ_k are empirically obtained closure coefficients.

There are two extensions to the $\kappa-\omega$ turbulence models, the mathematical details of which exceed the scope of this study. Both of these extensions also imply a higher computational cost. Nonetheless, despite the higher computational cost these models are being used widely for VAWT simulations, obtaining the closest results to experimental data [14] [13]. An insight on the computational cost of the turbulence models available on ANSYS Fluent can be seen in Figure 2.6.

The $k-\omega$ SST Model

The $k-\omega$ SST Model combines the $k-\omega$ and the $k-\varepsilon$ models, using the former for areas near the wall (such areas require a higher accuracy), and using the latter for free flow areas, taking advantage of the comparatively lower computational cost.

The Transition SST Model

Elaborating further on the the $k-\omega$ SST model, this model adds an equation for intermittency and another one for the transition criterion using the momentum thickness Reynolds number. Thus, this model simulates laminar sub-layers inside turbulent flows.

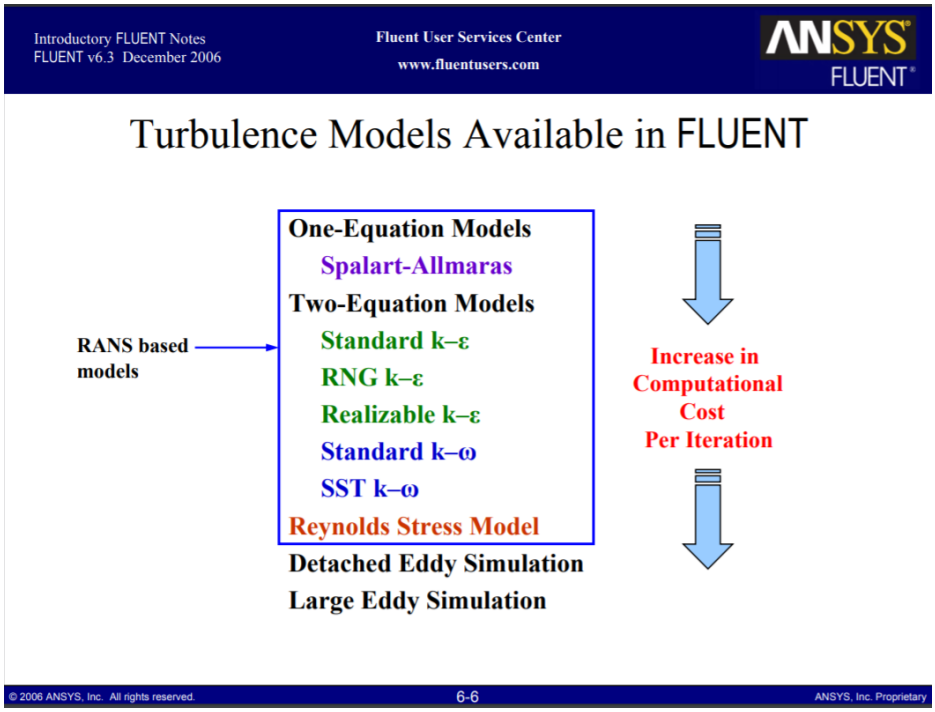

Figure 2.6 Turbulence models available in Fluent [15].

3 Motivation for further Dynamic Stall Study

As a merely urban application, H-rotors are an attractive solution in the low-kilowatt range due to their insensivity to yaw in the wind and turbulent flow, which is ever present in the wind shear conditions in rooftops, as well as their comparatively lower production costs. Nonetheless, their design makes the angle of attack (α) change constantly, with its range comprising $0 \leq \alpha \leq 2\pi$. Therefore, a sizeable amount of power is lost behind the airfoil post-stall, in vortical and swirling flow [16]. Moreover, dynamic stall can produce structural fatigue and noise. The latter is especially important in urban environments, and therefore regulated at a national and European level. The limit averages 40 dB for mixed-use areas [17].

Dynamic stall occurs mainly in relatively low TSR range ($\lambda = \frac{\Omega R}{V_\infty}$), namely $0.5 \leq \lambda \leq 3$. This is mainly due to lower Reynolds numbers on the blades than for high TSRs, a fact which means increased turbulence, as can be seen in Figure 3.1.

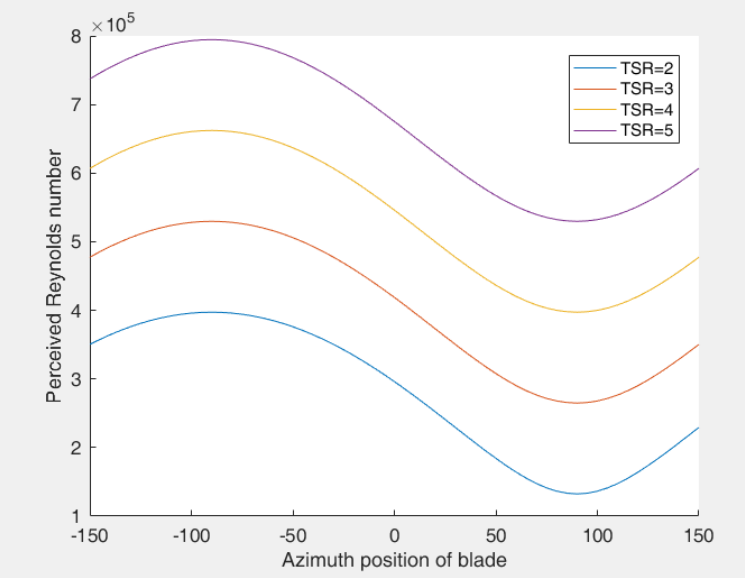

Figure 3.1 Influence of the Tip Speed Ratio on the Reynolds number.

Thus, VAWTs are normally operated in the higher TSR area, $4 \leq \lambda \leq 7$. Higher TSRs might imply higher noise levels and the higher rotational speeds might also raise safety concerns in residential applications. Higher TSRs might also yield comparatively lower power. As an example, Figure 3.2 illustrates the power coefficient (C_P) against the TSR, for a three-bladed H-rotor. The data in the graph was obtained with QBlade. The figure indicates that to achieve the maximum C_P, the turbine must be operating with TSR=2.7, but with larger TSRs, the power coefficient remains similar. It is past TSR=4 that the C_P plummets, and the turbine no longer producing energy.

It can be therefore asserted that for the turbine in the example, dynamic stall cannot be regulated merely through controlling the TSR.

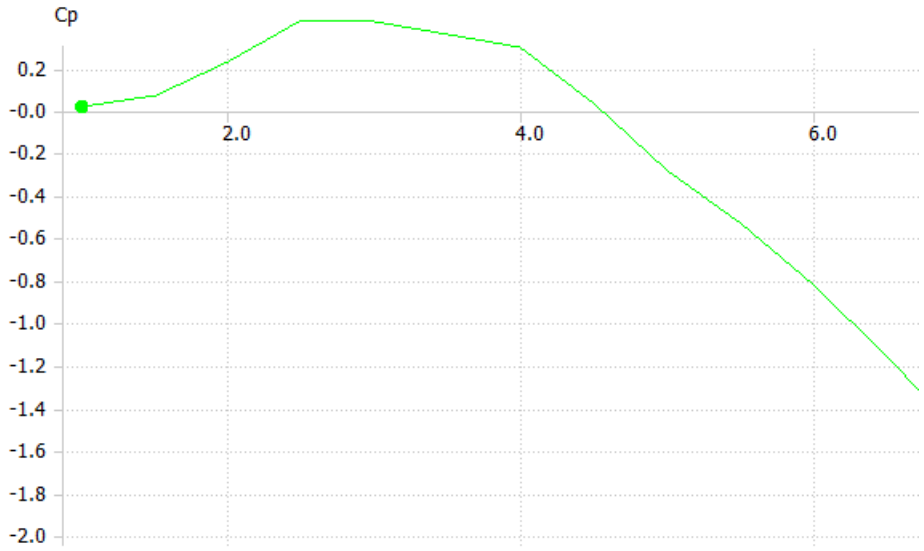

Figure 3.2 Influence of the Tip Speed Ratio on the power coefficient.

In order to alleviate detrimental effects produced by dynamic stall, several approaches have been taken. One of this approaches is implementing twisted airfoils (so at any point, the blade will have areas experiencing no stall, due to the change in the angle of attack along the blade). Twisted airfoils also flatten torque peaks, thus, lessening the sensitivity to structural problems. Nonetheless, structural complexity also implies higher upfront costs.

Active vortex generators, through synthetic jets is another approach. These approach is however, even if effective, more costly, and thus cannot offer a cheap means of energy to the domestic customer, both through low upfront and maintenance costs.

Inspired by aircraft aerodynamics, double airfoils were studied in [16], in order to simulate a wing and flap configuration. Sizeable improvements were found beyond raw performance results, such as the turbine being found to behave as a mix of a Darrieus and Savonius turbines, enabling self-start.

With the objective of improving the performance in the stall-sensitive operational ranges, but pursuing the highest degree of structural simplicity possible and therefore low production costs, passive measures on a single airfoil will be studied. These measures consist of a series of geometrical modifications in the airfoils, which will be part of simulations, thus measuring the performance improvement.

4 Airfoil Analysis

In order to analyse exclusively performance improvements when modifying the airfoil, the turbine configuration will remained unchanged through the testing phase. Its characteristics are summarised in Table 4.1.

Table 4.1 Turbine characteristics.

Number of blades (B)	3
Turbine height (h)	3m
Turbine radius (R)	1.5m
Airfoil chord (c)	0.25m

Turbine solidity also characterises the turbine and its overall performance, as referenced on [18]. Therefore, as finding an optimum for turbine solidity is out of the scope of this study, solidity will remain constant throughout the testing phase, for every airfoil modification. Solidity (σ) can be calculated through: $\sigma = \frac{Bc}{R}$, in this case thus yielding $\sigma = 0.625$.

4.1 Analysis Procedure using QBlade

4.1.1 Data Import and Polar Generation

Once the desired airfoil outline has been saved as a .DAT file, it can be imported into QBlade. The airfoil can then be analysed, but its polar data is needed before further steps.

QBlade has a built-in polar calculation algorithm, namely XFoil, but even if it is widely used within aerodynamics, this method is insufficient when calculating upon a highly irregular profile, for example the passive modifications encompassing this study. For these profiles, the polar can be imported directly into QBlade once it has been calculated through other means.

The settings for XFoil polar generation are as per Figure 4.1, and an example of polars viewed on QBlade is shown in Figure 4.2.

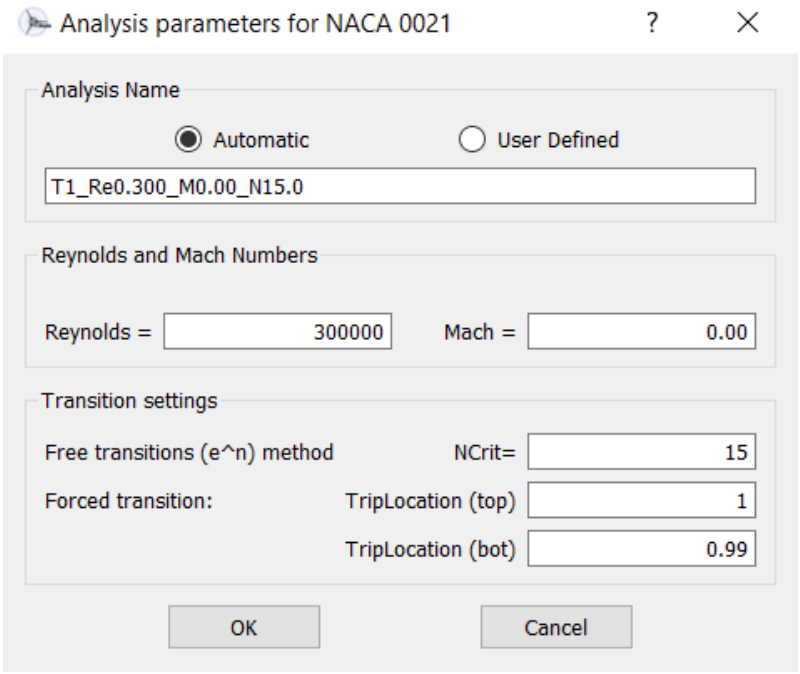

Figure 4.1 XFoil settings.

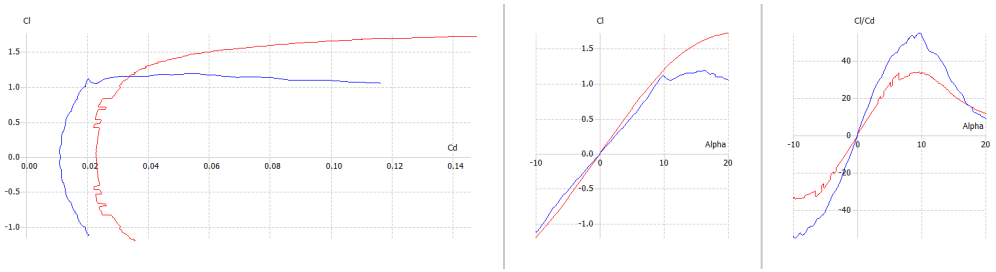

Figure 4.2 QBlade polar.

4.1.2 Polar Extrapolation

Given that a polar is usually calculated for a narrow range of angles of attack around 0°, the polar needs to be extrapolated for all angles of the azimuth. Two extrapolation methods are built into QBlade, the Viterna-Corrigan and Montgomery methods, the explanation of which is out of scope of this study. An example of this extrapolation is as per Figure 4.3.

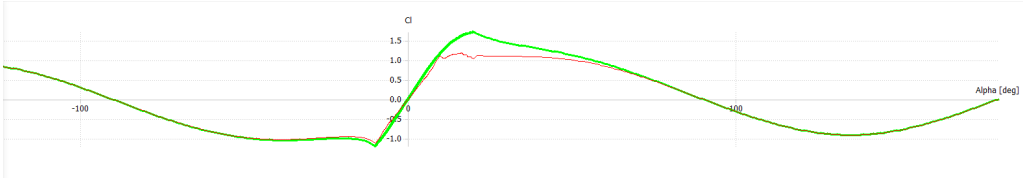

Figure 4.3 Viterna-Corrigan extrapolation.

4.1.3 Rotor Design

The already calculated polar extrapolation is then used to calculate further using the DMS and LLT theories. Before a simulation is undertaken, the rotor needs to be designed, assigning height, radius, profiles and blade twist, among others. The settings used for the base configuration are shown in Figure 4.4.

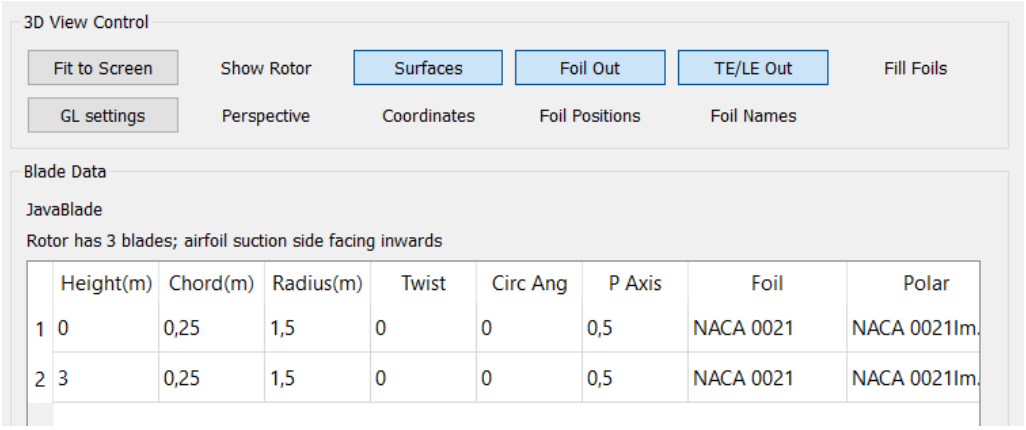

Figure 4.4 Rotor design, Base configuration.

4.1.4 Double Multiple Streamtube Simulation

For DMS simulation, once the rotor has been chosen, the only parameters to be chosen are the tip speed ratio range, the wind speed and a series of atmosphere parameters as per Figure 4.5.

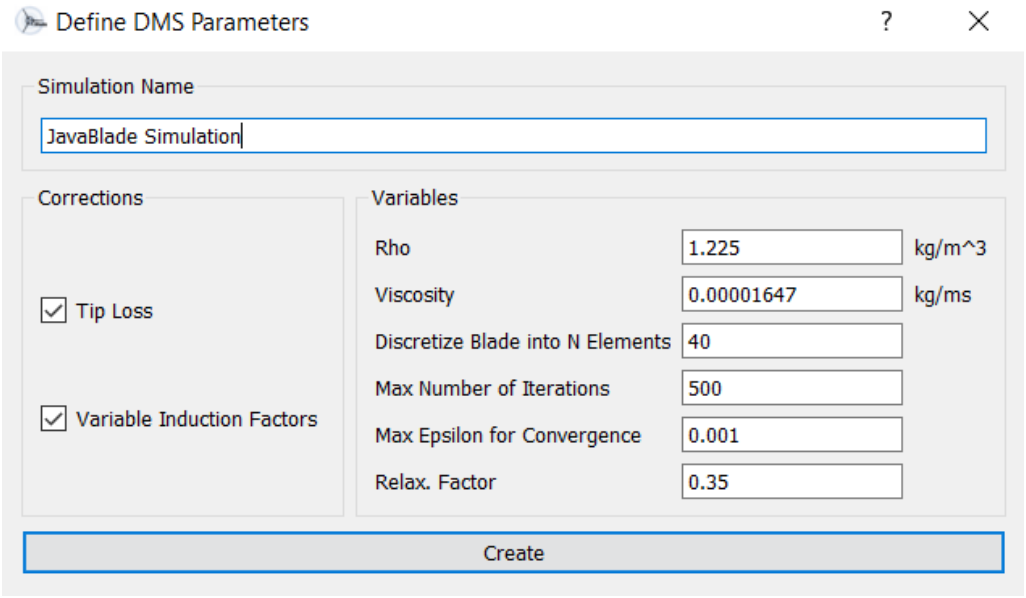

Figure 4.5 DMS, configuration parameters.

The result of a simulation under this theory and its shortcomings will be further discussed under the case studies for each turbine.

4.1.5 LLT Simulation

For a successful LLT simulation it is key to understand and adapt the wake and vortex modelling parameters. Their adaptation to this study will be discussed in the next section, Base Configuration. The setup screen for the Operational Point is as per Figure 4.6, and the one for the Output, Algorithm and Wake Parameters is as per Figure 4.7.

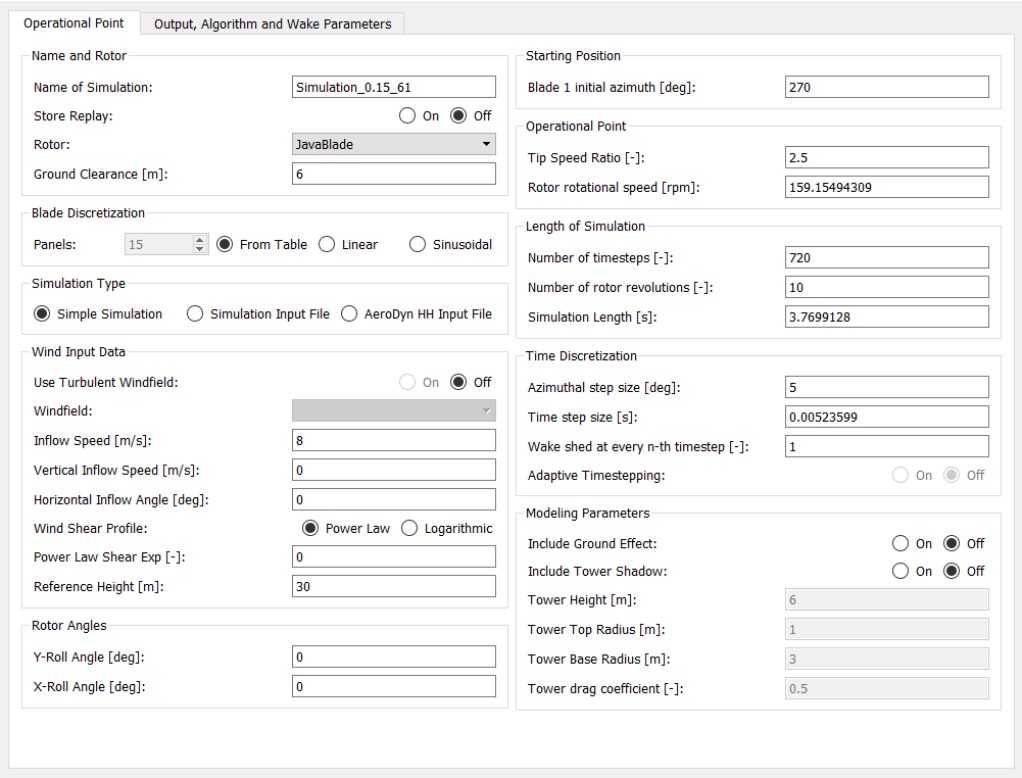

Figure 4.6 LLT, operational point.

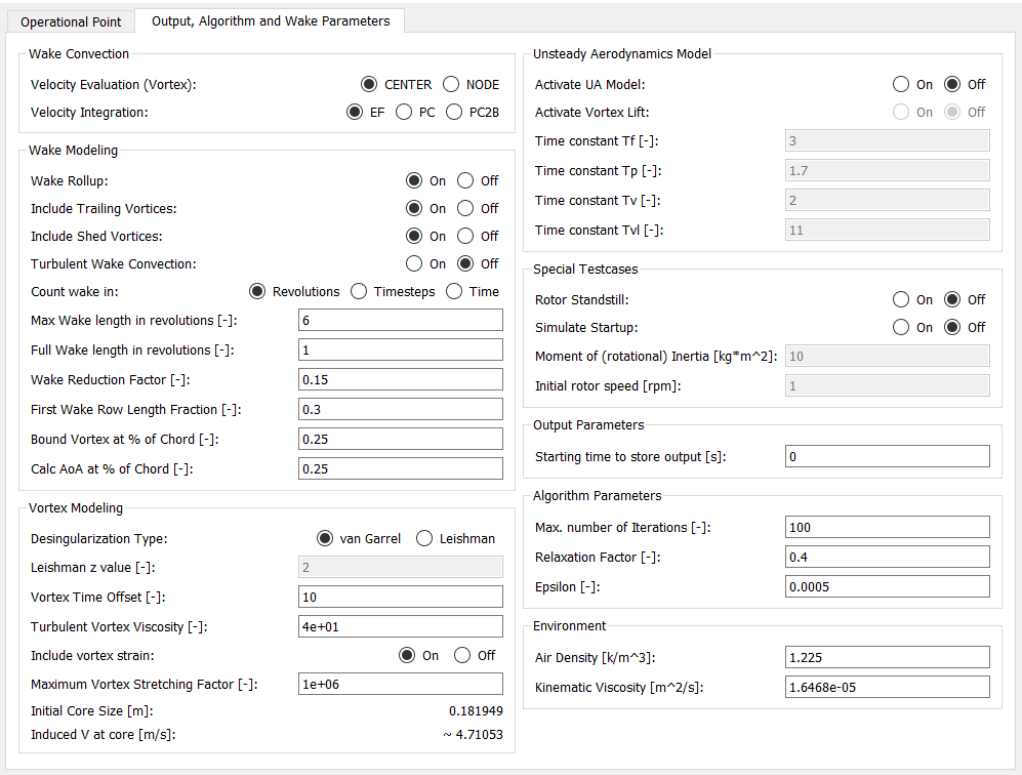

Figure 4.7 LLT, output, algorithm, wake parameters.

4.2 Base Configuration: the NACA 0021 airfoil

The NACA 0021 airfoil was chosen specifically due to its improved capability to operate under dynamic stall. For similarly-sized turbines as the case in this study, wind tunnel tests have been undertaken, comparing NACA0015 and NACA0021 airfoils, as well as changes in blade pitch and its influence on performance. Blade pitch changes are nonetheless out of the scope of this study.

The NACA 0021 airfoil is part of the NACA 4-digit series, developed by the National Advisory Commitee for Aeronautics (NACA) in the 1940s. The 4 digits define key features for the airfoil:

- The first digit defines relative camber, as a percent of the chord
- The second digit defines the relative distance of the maximum camber point from the leading edge, as a percent of the chord
- The last two digits define the maximum thickness of the airfoil, as a percent of the chord

For a given position along the chord (as a percent of the chord), the local half thickness is given by:

$$y = 5t[0.2969\sqrt{x} - 0.1260x - 0.3516x^2 + 0.2843x^3 - 0.1015x^4] \tag{4.1}$$

Thus, points can be calculated in order to plot the airfoil as a first step. These values are illustrated on Appendix A.1.

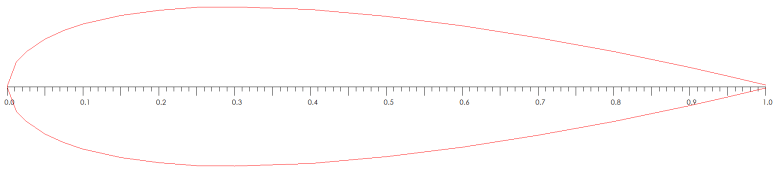

Figure 4.8 NACA0021, clean airfoil.

Under null pitch conditions, [19] showed that the point of $C_{P_{max}}$ for the NACA0015 airfoil was given for $\lambda = 1.6$, while for the NACA0021 airfoil, $C_{P_{max}}$ would be obtained at $\lambda = 1.45$. It was speculated that a lower value for λ could therefore be linked with a more adequate dynamic stall performance.

Furthermore, in the same study, it was determined that with a higher blade pitch (namely $\beta = +7.8\,\text{deg}$), the turbine featuring a NACA0021 airfoil was still able to yield power in spite of dynamic stall. In the meantime, under the same conditions, such a blade pitch surpassed the operational conditions for the NACA0015 airfoil. This phenomenon could as well be justified by improved dyamic stall performance.

As a state-of-the-art analysis, most present day studies on VAWTs and dynamic stall are being undertaken on several NACA airfoils, for the most part NACA0012 and NACA 0018. The NACA0015 airfoil would then be at an intermediate point, in terms of performance.

After entering data for the NACA0021 airfoil on QBlade, the airfoil polars were also generated through this same tool. QBlade uses XFoil as its airfoil generator. Its using XFoil will pose problems later, as XFoil is unable to converge for complicated geometries, and another airfoil generator, namely JavaFoil, was found.

XFoil Polars

As generated by QBlade, the C_l plotted against C_d and C_l plotted against α can be seen on Figures 4.9 and 4.10, respectively. It can be seen that for null C_l, C_d equals 0.17 and C_d rockets for $C_l = 1.1$. This increase in drag coefficient can be attributed to the occurrence of stall on the airfoil, as is shown on Figure 4.10.

Moreover, using these polars QBlade calculates the power and torque coefficients. These values are illustrated on Figures 4.11 and 4.12. The latter is of special interest, as it shows the least favourable azimuth, at which dynamic stall is most present, producing negative torque, and therefore power, on the turbine. On the former, it is seen that the maximum power coefficient value is 0.52. This is a highly irrealistic value which shows the overestimation expected due to the use of the DMS theory.

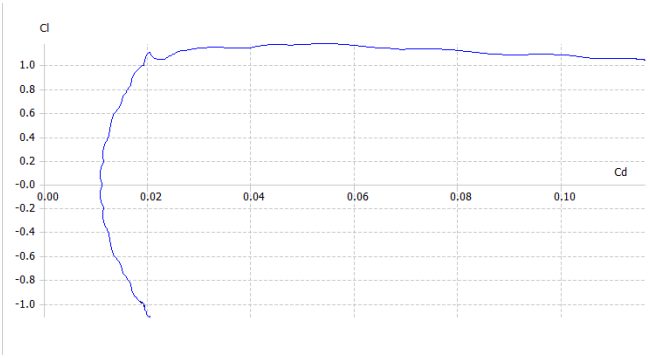

Figure 4.9 C_l against C_d, clean configuration, XFoil.

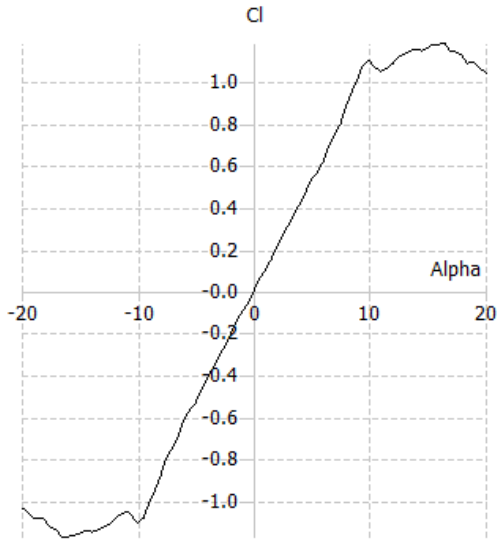

Figure 4.10 C_l against α, clean configuration, XFoil.

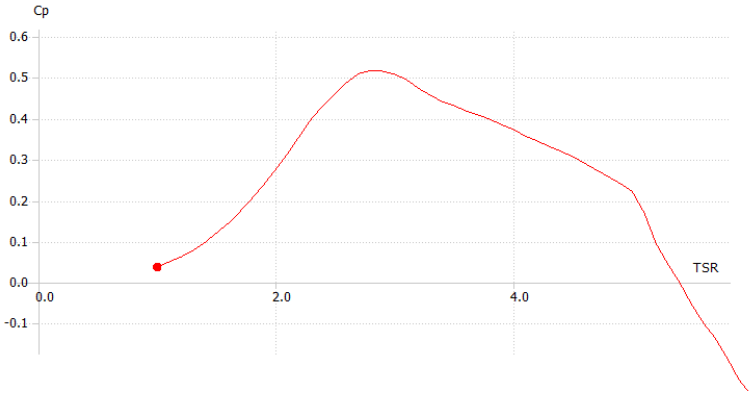

Figure 4.11 C_P against λ, clean configuration, XFoil.

JavaFoil Polars

JavaFoil was also used for additional airfoil polar calculation. JavaFoil[20] first determines the velocity distribution through a panel method. This panel method divides the airfoil into multiple straight panels, with each inducing unknown velocities on themselves and others. These velocities are then calculated through a system of linear equations. Here, a boundary condition is that the velocities are always tangent to the

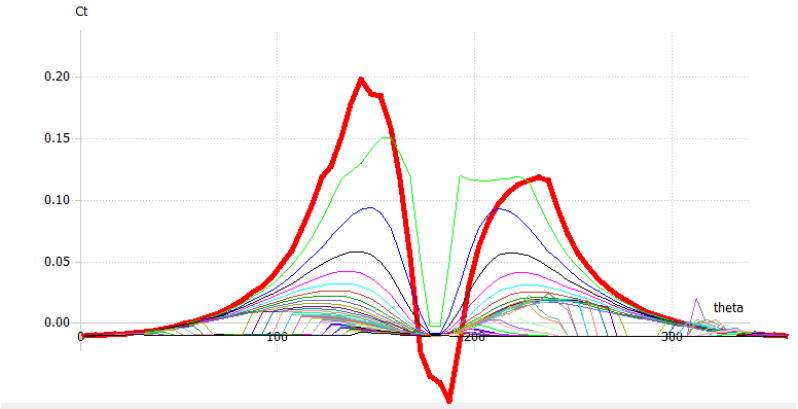

Figure 4.12 C_t against θ, clean configuration, XFoil.

panels.

Later on, a viscous boundary layer analysis is undertaken, so as to calculate the friction drag, as well as lift, drag and moment corrections in case of flow separation.

JavaFoil obtained fairly similar polars to those obtained by XFoil. These JavaFoil polars were then also used by QBlade to calculate similar performance coefficients, when compared to the XFoil case. These polars and values can be seen on Figures 4.13, 4.14, 4.15 and 4.16. Irregularities in the polars can be seen in these Figures, and also a post-processed alternative. Peaks and buckets in the graphs were smoothed out using MATLAB (see List of Codes), using a 4th-degree polynomial best fit. These irregularities in the polars can be attributed to convergence problems during polar generation. Post-processed polars shall be used for further analysis.

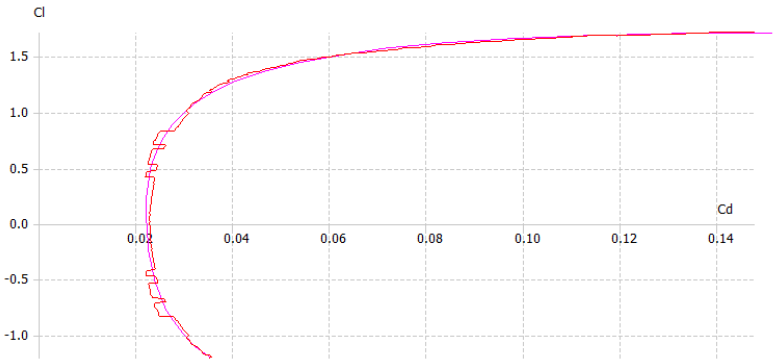

Figure 4.13 C_l against C_d, clean configuration, JavaFoil.

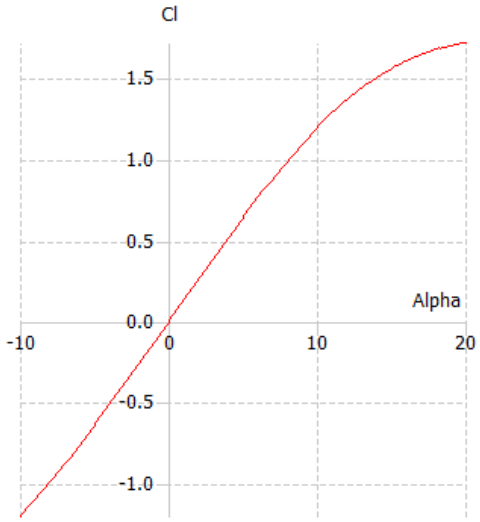

Figure 4.14 C_l against α, clean configuration, JavaFoil.

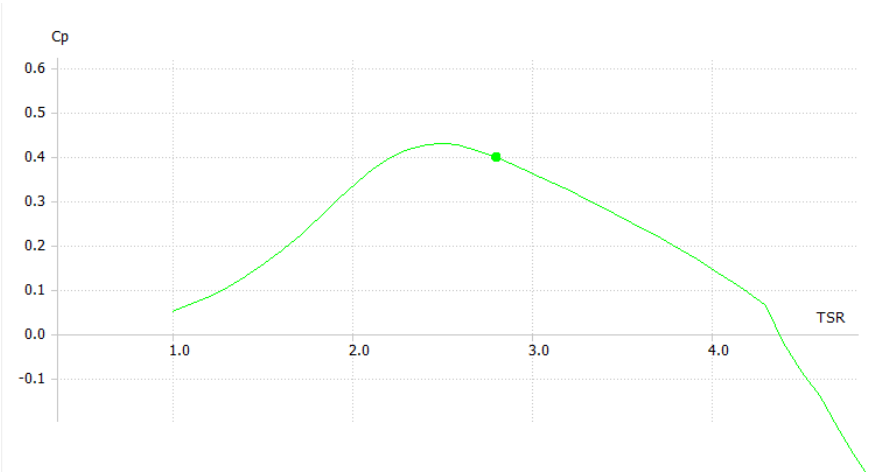

Figure 4.15 C_P against λ, clean configuration, JavaFoil.

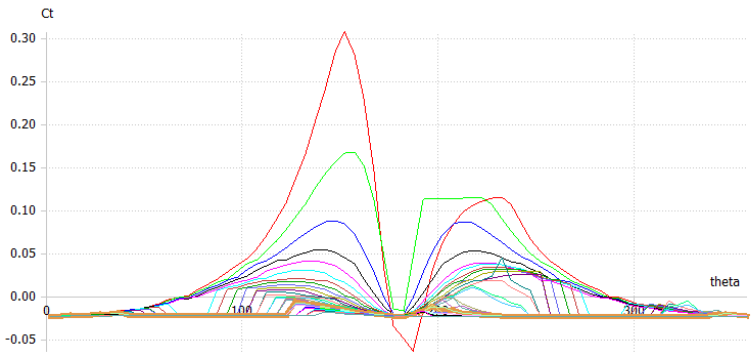

Figure 4.16 C_t against θ, clean configuration, JavaFoil.

Lifting Line Parameter adaptation The Lifting Line Theory method was used to simulate a regular load case, with $\lambda = 2.5$ and constant wind speed $V_w = 8m/s$, obtaining $C_P = 0.38$.

Problems were found while making use of the LLT method, as calculations are highly sensitive to its vortex parameters. Parametres have to be adapted to each user case and turbine. The programme developer validates the LLT in [21], analysing sensitivity to certain vortex modeling parametres. These tests (Figures 4.17 and 4.18) showed that a maximum wake age of 6 revolutions and a full wake age of 1 revolution is offers a good balance in terms of calculation time and accuracy.

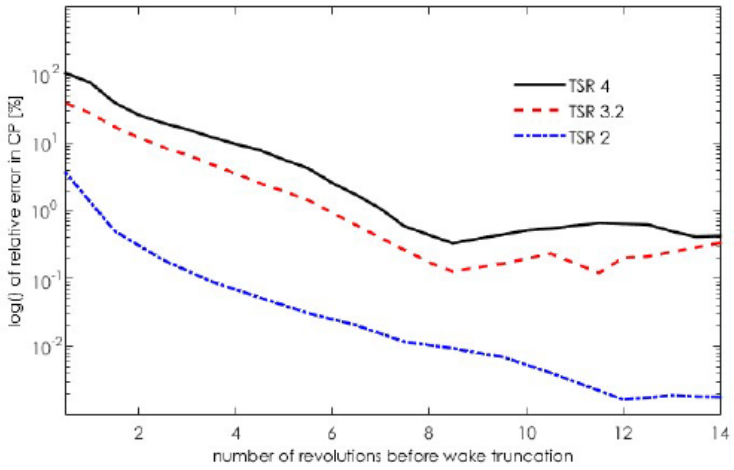

Figure 4.17 Effect of maximum wake age on C_P accuracy [21].

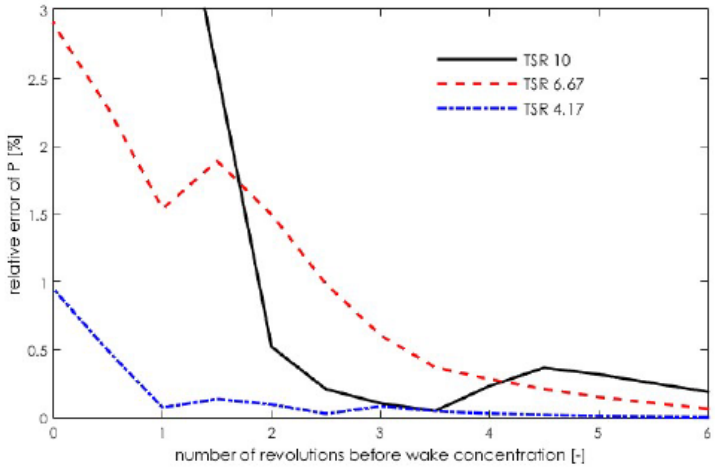

Figure 4.18 Effect of full wake age on C_P accuracy [21].

Wake reduction will also be analysed. Wake reduction intends to reduce computation time by truncating the vortices with the lowest circulation. Simulations were undertaken on QBlade and as can be seen on Figure 4.19, the best results can be seen for vortex reduction 0.2 and 0.15, in terms of stability and convergence. Even though the results for vortex reduction nearest to 0 are the most accurate, it can be seen that they fluctuate and do not converge in a meaningful manner within the simulation time (10 revolutions), so for a preliminary analysis higher wake reduction proportions are more appropriate.

Even though the LLT method uses more sophisticated calculations, it depends heavily on a well-calculated polar, which is a problem for VAWT, as θ ranges from 0 to 2π. These C_P values calculated by the DMS and LLT methods should just taken as trend, serving as an orientation through this early stage of the study. The reason is that typical C_P values for Darrieus turbines are usually in the 0.3-0.4 range. This sort of discrepancy between results yielded by LLT-DMS theories and CFD could also be seen on Figure 2.5. For the aforementioned parameters, LLT analysis yields $C_P = 0.383$ (Figures 4.20 and 4.21), which is closer than DMS to the expected value to be given by CFD, alas, lower.

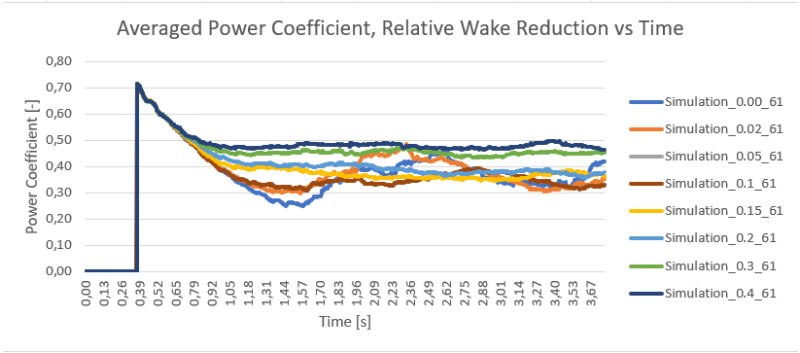

Figure 4.19 C_P against wake reduction, clean configuration, JavaFoil.

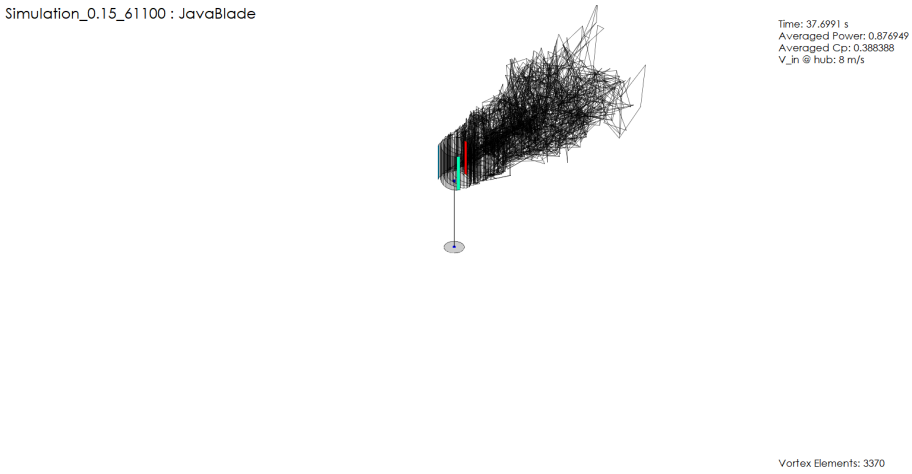

Figure 4.20 C_P for $\lambda_{C_{Pmax}}$ at final status, clean configuration (LLT), JavaFoil.

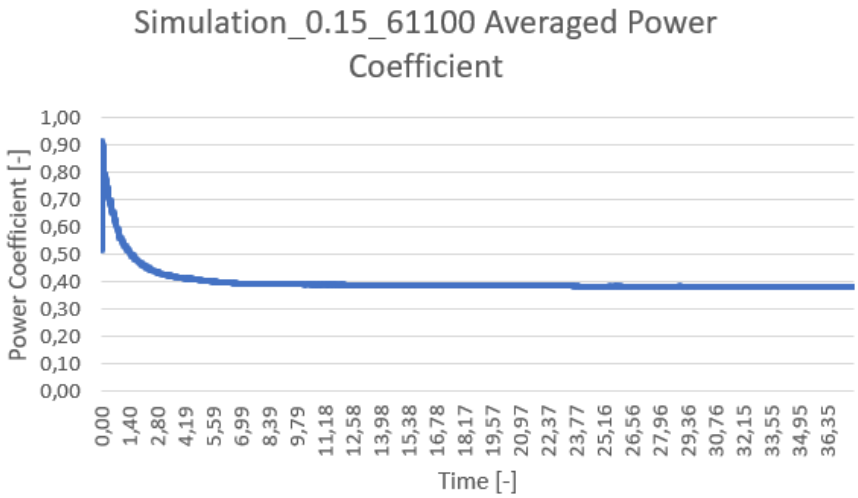

Figure 4.21 C_P for $\lambda_{C_{Pmax}}$ vs time, clean configuration (LLT), JavaFoil.

4.3 The Gurney flap

The Gurney flap is a structurally simple device, made up of a short strip, which is placed perpendicularly to the chord line of an airfoil, near the trailing edge. This device was first developed by Gurney for motorsports applications, being later on used for aerospace operation. The Gurney flap is said to break the Kutta boundary flow condition, as it creates a pair of contrarotating vortices in the immediate vicinity of the flap, which makes for an altered trailing edge circulation [22].

Liebeck studied the device and found best results with a height comprising 1.25% of the chord, as a compromise between lift and drag for the studied airfoil. Drag increases exponentially for heights greater than 0.02c. Multiple cases were studied:

- 2%c height, placed 90%c from the front of the airfoil: 90200
- 2%c height, placed 95%c from the front of the airfoil: 95200
- 1.25%c height, placed at the rear of the airfoil (100%c): 100125
- 1.25%c height, placed 95%c from the front of the airfoil: 95125

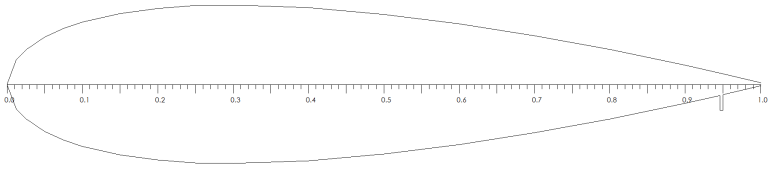

Figure 4.22 Gurney flap-modified NACA0021 airfoil.

The polars (obtained through JavaFoil, as the XFoil method cannot converge satisfactorily under the given geommetry) and the values calculated by QBlade are illustrated by Figures 4.23, 4.24, and 4.25.

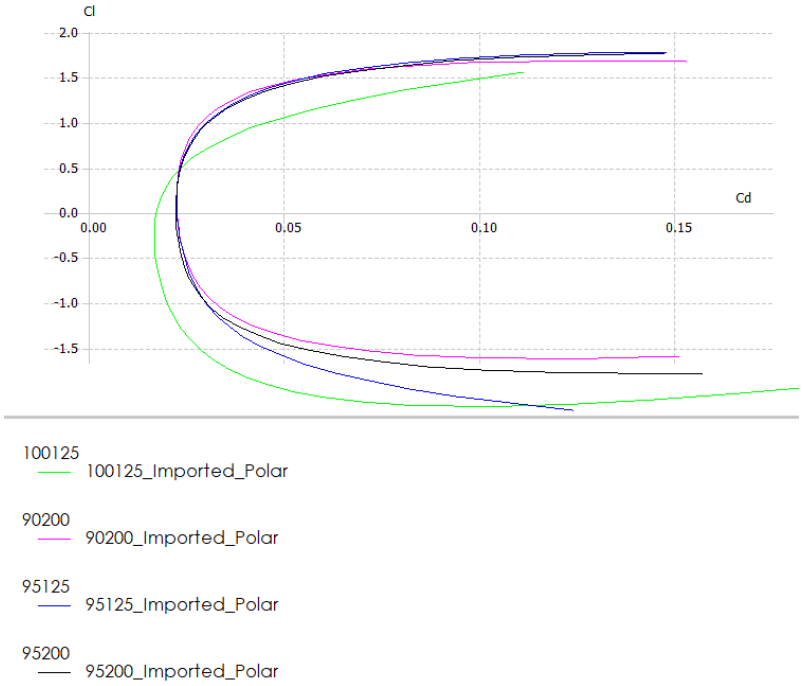

Figure 4.23 C_l against C_d, Gurney flap-modified airfoil.

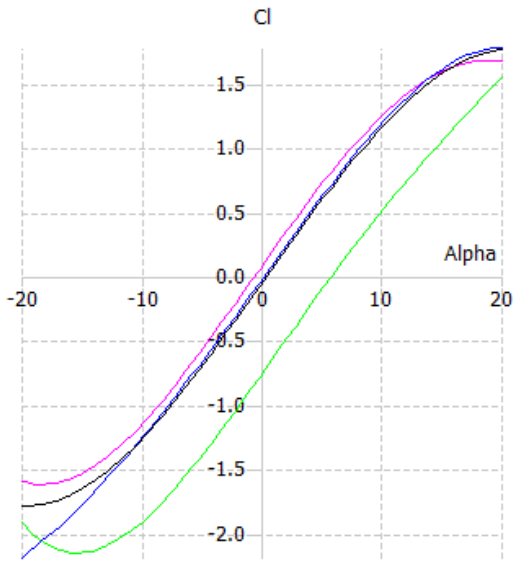

Figure 4.24 C_l against α, Gurney flap-modified airfoil.

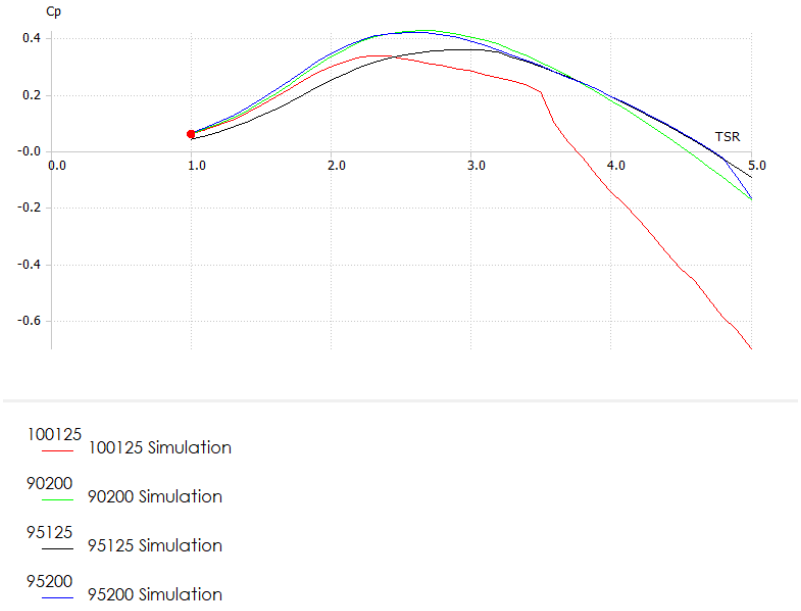

Figure 4.25 C_P against λ, Gurney flap-modified airfoil.

Even though the calculated maximum C_P remains similar to the clean configuration, this may be due to the nature of the calculation of the polar and its further computation on QBlade, as the DMS theory does not take dynamic stall into consideration, and the performance improvement that such devices would provide. Nonetheless, it can be seen that $\lambda_{C_{P_{max}}}$ is lower than for the clean case, and that the curve is overall flatter. This might mean that the effects of dynamic stall are no longer as strong.

Out of all the tested Gurney flap configurations, 2% heights performed best. A 0.95c placement can be speculated to be the most beneficial, as the C_P decreases comparatively more slowly, while rising faster in the low λ range. Thus, the Gurney flap-modified **95200** airfoil will be used for further analysis.

The plot details of such an airfoil are summarised in Appendix 4.2.

Meanwhile, Lifting Line Theory analysis yielded $C_P = 0.461$, as per Figures 4.26 and 4.27. This would imply a performance improvement of 20.3%, relative to the already studied clean configuration case. This is the largest improvement out of all devices studied.

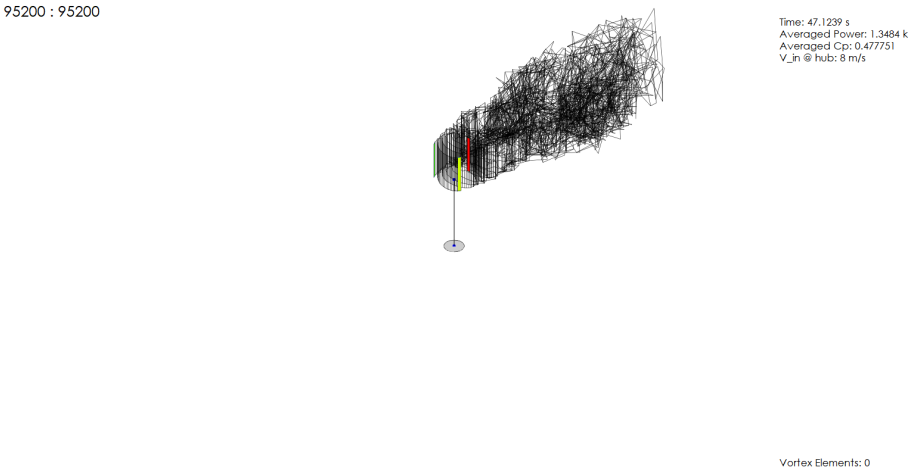

Figure 4.26 C_P for $\lambda_{C_{P_{max}}}$, Gurney flap-modified airfoil (LLT).

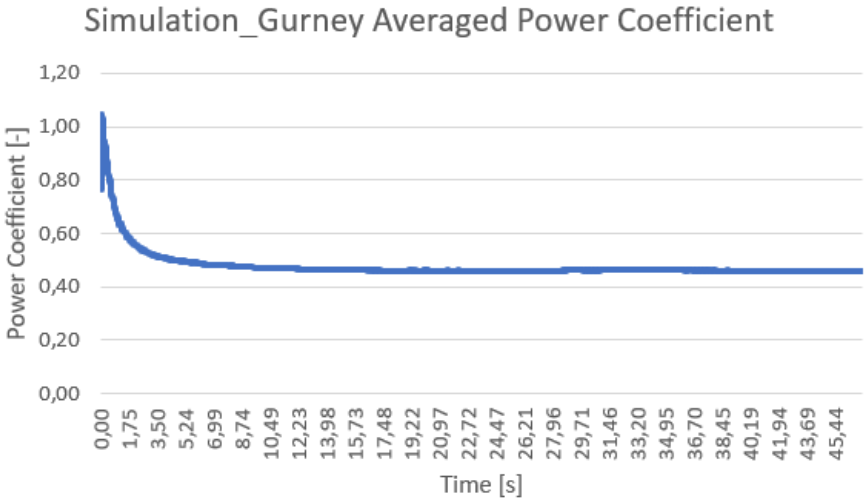

Figure 4.27 C_P for $\lambda_{C_{P_{max}}}$ vs time, Gurney flap-modified airfoil (LLT).

4.3.1 The T-strip

The T-strip consists of a double Gurney flap, on both upper and lower surfaces along the trailing edge, forming a T-shaped section (hence the name). An airfoil was generated featuring a $h = 0.0125c$ T-strip. Two options were considered, one featuring flaps perpendicular to the centreline, and another with flaps perpendicular to the airfoil surface. An overall view of these modifications is as per Figure 4.28, see Figure 4.29 for further details.

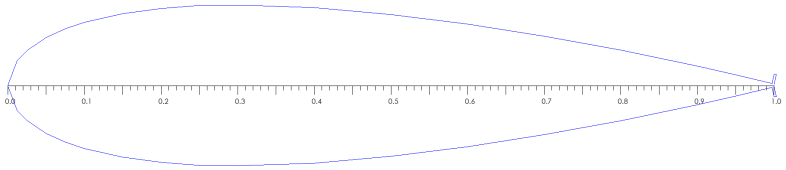

Figure 4.28 T-strip-modified NACA0021 airfoil.

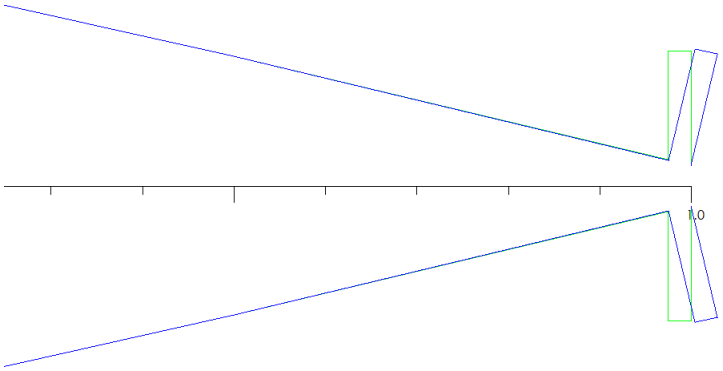

Figure 4.29 Detailed view, T-strip-modified airfoil.

Polar details are as per Figures 4.30 and 4.31, two cases being studied:

- T-strips placed perpendicularly to the airfoil centreline: 100125
- T-strips placed perpendicularly to the airfoil surface: Tstriptilt

It can be asserted that even if the lift coefficient is improved when compared to the base configuration, this comes with increased drag. This drag increase nullifies any lift improvement, and the power coefficient decreases from the base case. Power coefficient data is as per Figure 4.32. As best power coefficient results are obtained for the T-strip-modified airfoil which features t-strips perpendicular to the airfoil centreline (**100125**), this airfoil will be the one used for LLT analysis. Plot details on this airfoil are as per Appendix 4.4.

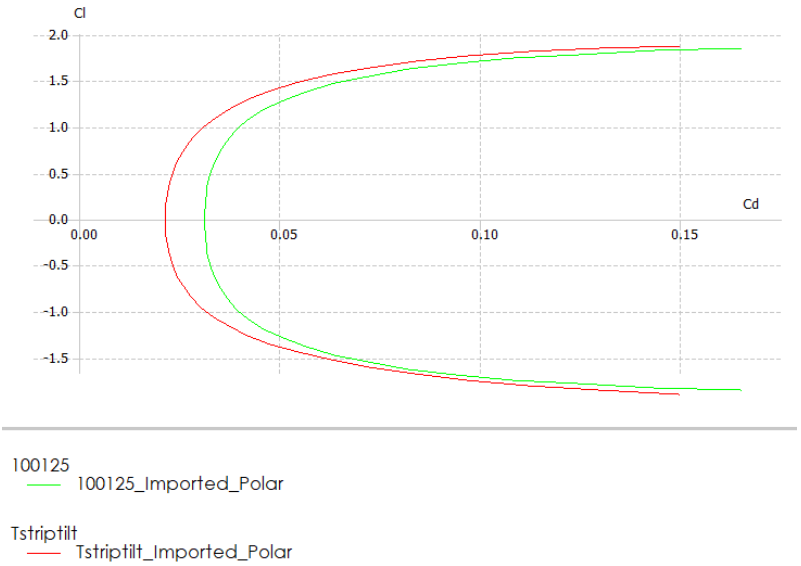

Figure 4.30 C_l against C_d, T-strip-modified airfoil.

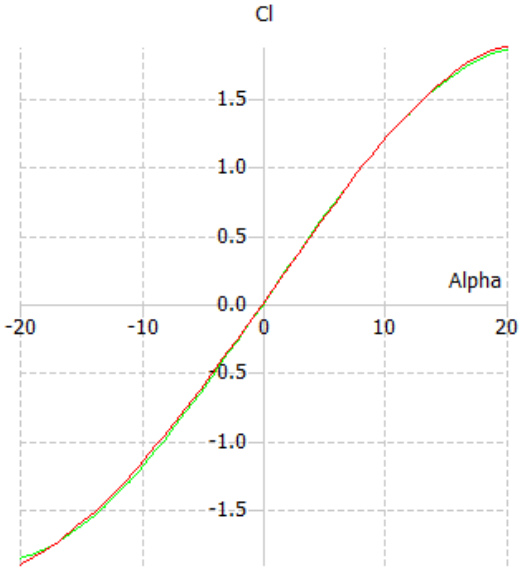

Figure 4.31 C_l against α, T-strip-modified airfoil.

Meanwhile, as can be seen in Figures 4.33 and 4.34, Lifting Line Theory analysis yielded $C_P = 0.372$. This result points toward a negative effect on performance, when compared to the clean case. This negative effect was also analysed with CFD for high TSRs on [23]. Therefore, this airfoil modification will not be selected for further CFD analysis on this project. Nonetheless, it could be so that a configuration of an asymmetrical T-strip could be effective, in which flaps on each airfoil size are differently sized. Due to the computational cost of such a parametric undertaking, this option is out of the scope of this study.

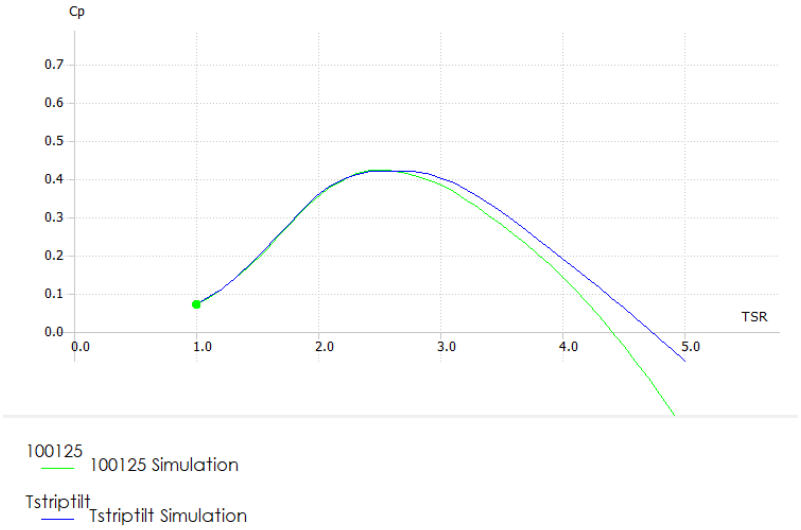

Figure 4.32 C_P against λ, T-strip-modified airfoil.

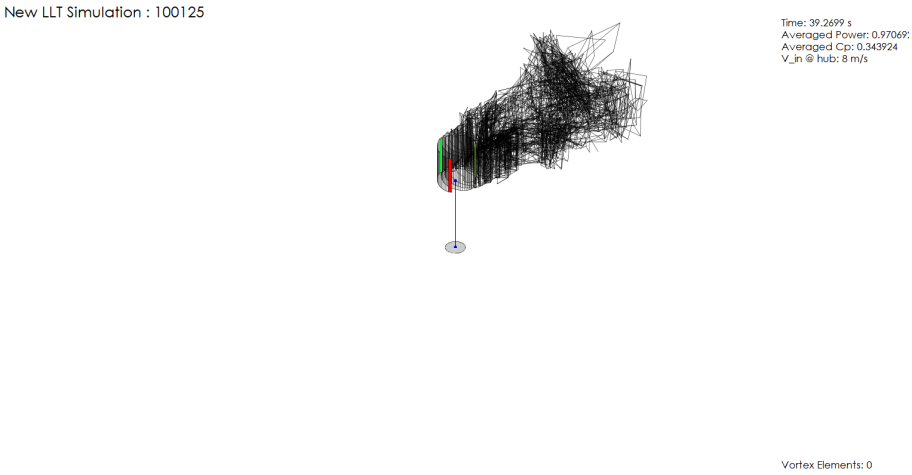

Figure 4.33 C_P for $\lambda_{C_{P_{max}}}$, T-strip-modified airfoil.

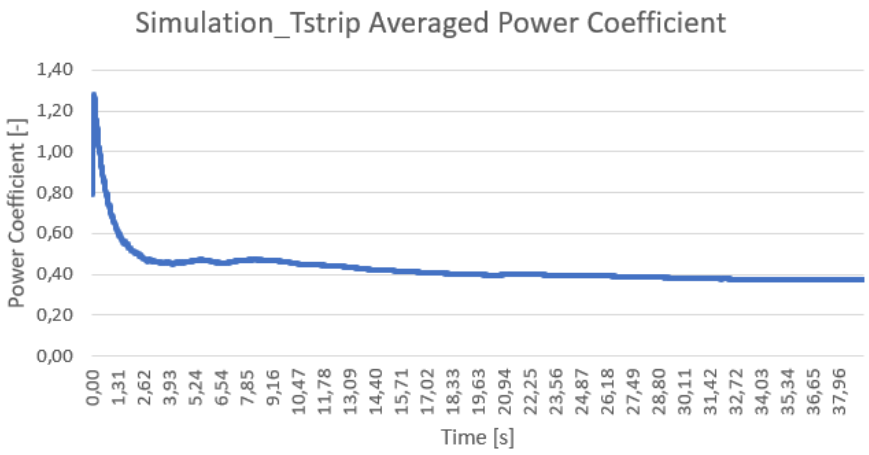

Figure 4.34 C_P for $\lambda_{C_{P_{max}}}$ vs time, T-strip-modified airfoil.

4.4 The stepped airfoil

Stepped (also called notched) airfoils were studied by Finaish and Witherspoon in [24], applied to a NACA 0012 profile. These airfoils feature a perpendicular cut in the surface (upper surface in this study), extending downstream. Such devices were found to enable lift augmentation through the induction of vortices in the steps, the best results being found for steps extending from $x = 0.5c$ to $x = 0.75c$. The lift-to-drag ratio was also noticeably improved. These improvements on the lift-to-drag ratio and overall lift can be seen on Figures 4.36 and 4.37. Power coefficient improvements were found using the DMS theory (Figure 4.38), especially in very low TSRs (around TSR=1).

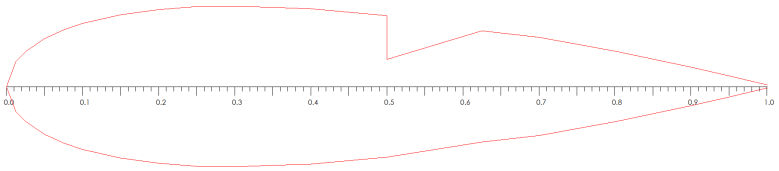

Figure 4.35 Stepped NACA0021 airfoil.

The plot details of the stepped NACA 0021 airfoil are as per Appendix A.5.

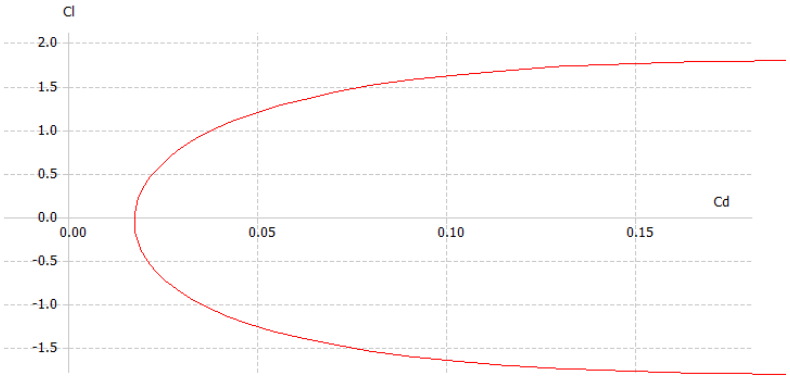

Figure 4.36 C_l against C_d, Stepped airfoil.

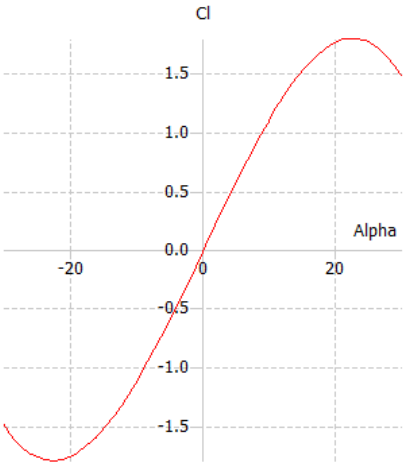

Figure 4.37 C_l against α, Stepped airfoil.

Meanwhile, Lifting Line Theory analysis yielded $C_P = 0.399$ (a relative performance improvement of 4.2%), as per Figure 4.39. Even if the improvement is small for the operational point, a stepped airfoil is especially interesting for dynamic stall situations at lower TSRs as previously mentioned. For low TSRs, the C_P is noticeably higher than for previous devices or the clean configuration.

Similar low-TSR performance improvements were also found by Frunzulica et al. for a NACA 0018 airfoil through CFD analysis [25]. Therefore, due to these proven low-TSR performance improvements, the studied stepped airfoil will be further analysed using CFD, along with the Gurney flap-modified airfoil, for its optimal TSR=2.5.

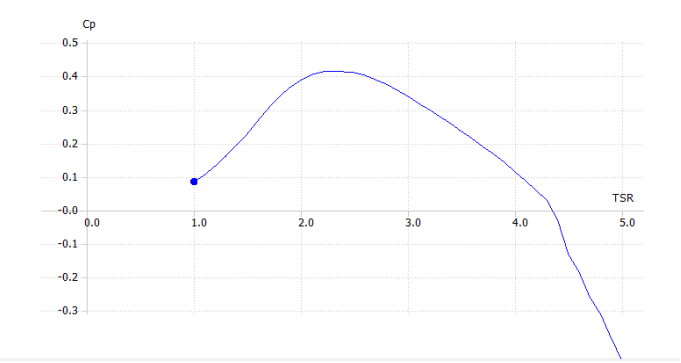

Figure 4.38 C_P against λ, Stepped airfoil.

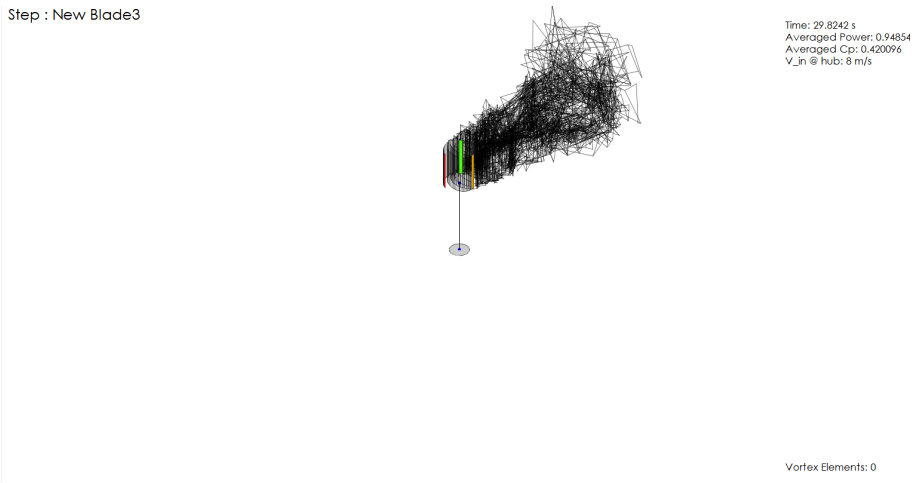

Figure 4.39 C_P for $\lambda_{C_{P_{max}}}$, Stepped airfoil (LLT).

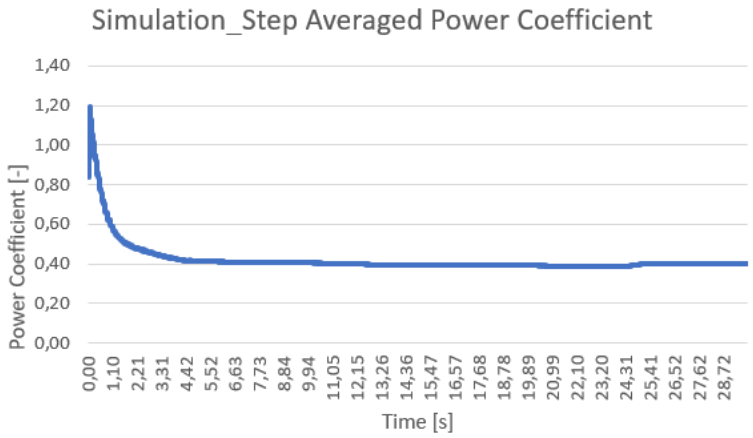

Figure 4.40 C_P for $\lambda_{C_{P_{max}}}$ vs time, Stepped airfoil (LLT).

A double-stepped airfoil was also taken into consideration in the early stages of this project in order to analyse lift improvements for the whole azimuth range, but polar calculation was highly unstable for this configuration, and no results of satisfactory quality were obtained.

5 CFD Simulation

In order to verify the quality of the calculations already undertaken using the Lifting Line Theory, the next step is to use ANSYS Fluent to apply Computational Fluid Dynamics to the designed profiles.

ANSYS Fluent was chosen for this project because it offers a comparatively shorter learning curve, as it provides the user with a simple graphical interface and configuration wizards.

5.1 Simulation Procedure

5.1.1 Design Modelling

It is understood that to simulate the rotation of the turbine about a z-axis, the overall mesh needs to be decomposed into a static part and a sliding mesh, which rotates about the desired axis. Lanzafame et al. [14] showed that a sliding ring mesh containing the 3 blades, and of the least thickness possible would provide the most stable results. A sliding ring also simulates a VAWT closest to the experimental situation. Conversely, a larger domain does not increase the quality of the simulation or the validity of the result when compared to the domain size to be used in this project, but just increases computation time. In Figure 5.1 a detailed view of the simulation domain used in this project can be seen.

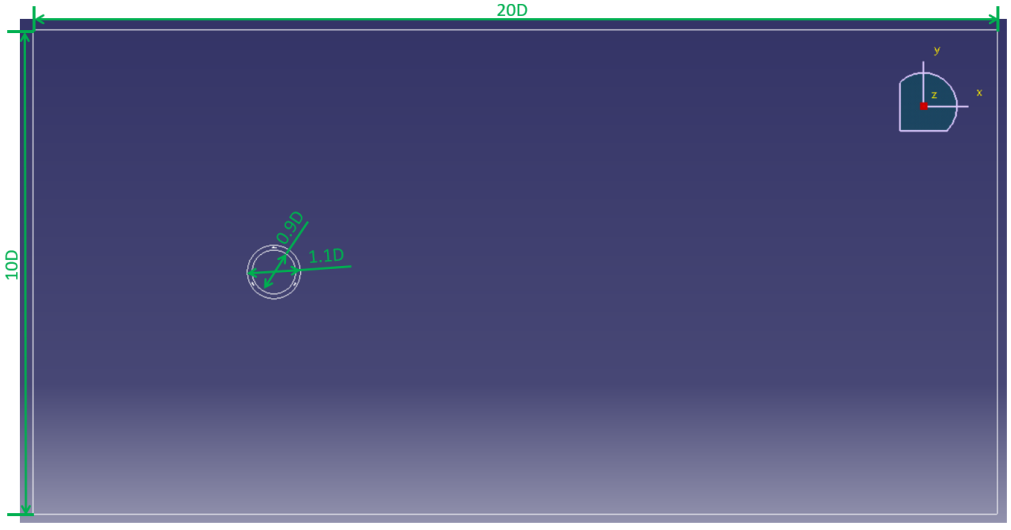

Figure 5.1 Simulation domain, detailed view.

1. The first step was to import the airfoil data from MS Excel to CATIA V5 using built-in macros, and then turn the sketch into a solid part. This way, CATIA V5 can calculate the inertia parameters, of which the centre of gravity coordinates are most important. These data, as applied to the clean configuration, are as per Figure 5.2.

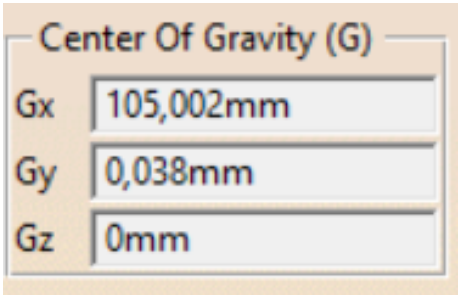

Figure 5.2 Centre of gravity coordinates, clean configuration.

2. The first blade was then put into place using these coordinates, aligning the CoG with the centre of coordinates and then displacing the blade 1500mm along the y-axis (the turbine radius). This process produces the result shown on Figure 5.3.

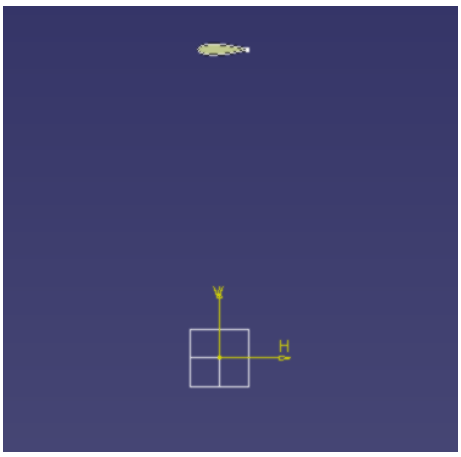

Figure 5.3 Displaced single blade, clean configuration.

3. In order to model the two remaining blades, a rotational pattern was set up, offsetting the blades 120 degrees. Turbine dimensions are measured from the turbine z-axis to the blade center line. The ring (0.2*Diameter thick around the turbine radius circumference) was created next using the dimensions as per Figure 5.4, and using boolean operations it was filled as a solid, and the blades emptied.
4. The last steps were to sketch and fill the inner and outer static domains, with dimensions as shown on Figure 5.1.

Subsequently, the model could be said to be ready for implementation, and the CATIA product file was imported into ANSYS DesignModeler. The three parts (ring, outer domain and inner domain) were imported separately, and then joined in DesignModeler using the Form New Part command.

As a last step in the whole modelling phase, the Shared Topology Method was set as None within the individual parts and as Automatic for the general part, and the material as Fluid. The shared topology method is key for this study, as setting it to none allows for interfaces to be formed between the different meshing components. The model is seen as per Figure 5.4 on DesignModeler.

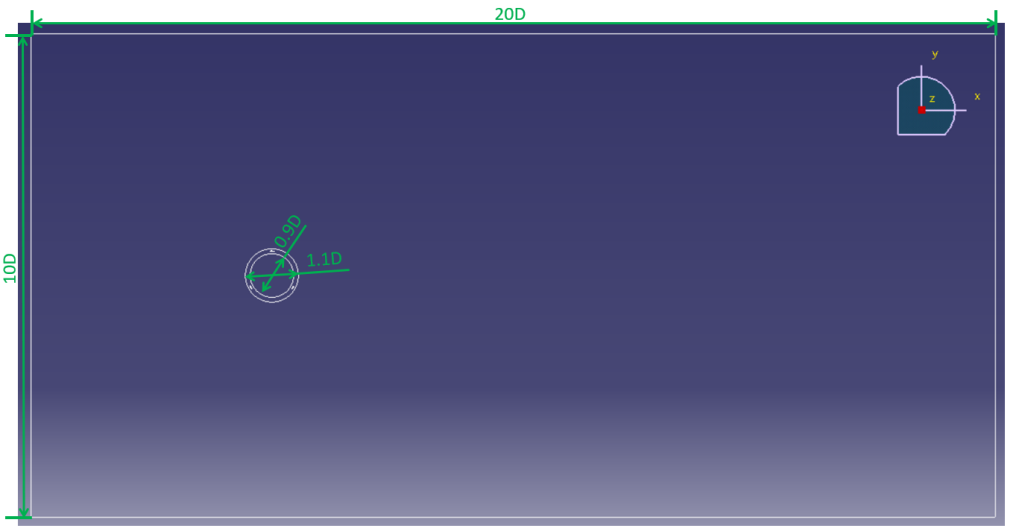

Figure 5.4 Simulation domain, DesignModeler.

5.1.2 Meshing

Meshing plays a crucial role in a CFD simulation, as a bad mesh can make the simulation not be representative. Thus, special care needs to be taken for meshing methods and their quality indicators.

First of all, Named Selections have to be set up, so that boundary conditions are easier to deal with. The Named Selections set up for this study are:

- The velocity inlet upstream of the turbine, named ”inlet”,
- The pressure outlet downstream of the turbine, named ”outlet”,
- The 3 blades of the turbine, named ”blade1”, ”blade2” and ”blade3”
- The outer fluid domain, named ”exterior”,
- The inner fluid domain, named ”interior”,
- The sliding ring area, named ”corona”,
- Within these 3 domain areas, two interfaces, ”interface1” between ”exterior” and ”corona”, and ”interface2” between ”corona” and ”interior”. Each of the interfaces is made up of two Named Selections, for each side of the interface belonging to each fluid domain.

The following steps have been taken for meshing:

- Edge Sizing for all 3 blades: $ElementSize = 10^{-3}m$. This allows for higher resolution along the blades, so that blade contours are correctly represented.
- Meshing Method: All Triangles Method. Either square or triangular mesh is implemented in ANSYS Fluent. A triangular mesh needs less time to be produced, which is key when undertaking CFD simulations with a personal computer.
- Inflation layers around all 3 blades: $FirstLayerThickness = 3.82 * 10^{-5}m$. This parameter adds parallel layers to the blades, which model the boundary layer next to them. The given first layer thickness was calculated using a yplus calculator, knowing that $y+ < 1$ (or in its range) for the turbulence models used for simulation. Furthermore, the inflation was set to 20 layers at a growth rate of 1.1, also used on [14]. A detail of said inflation layers can be seen on Figure 5.5.
- Face sizing: changes the mesh coarseness within the chosen domain area. Element size was chosen 0.05 m for the ”corona” area and 0.1 m for ”exterior”. Otherwise, the model was meshed as per the general element size, which was set at 0.5 m.

The overall mesh thus would look similar to that on Figure 5.6. A closer look into the turbine area is shown by Figure 5.7.

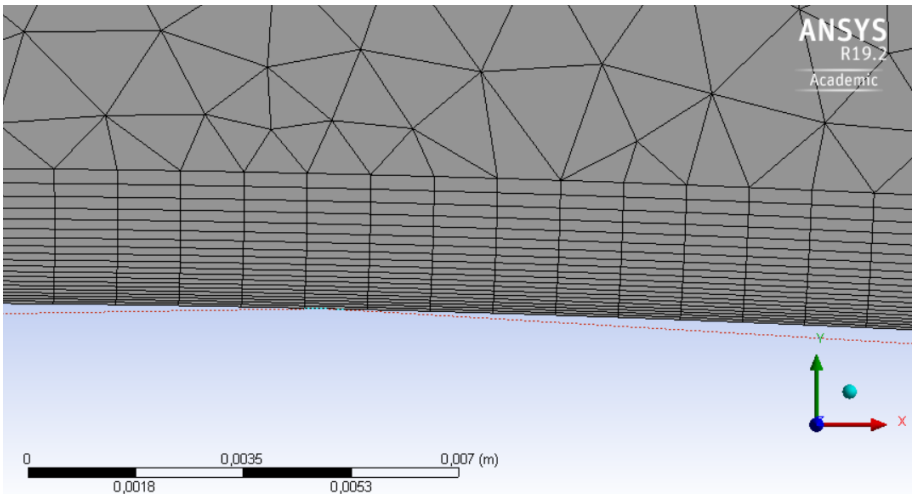

Figure 5.5 Inflation layers around a blade.

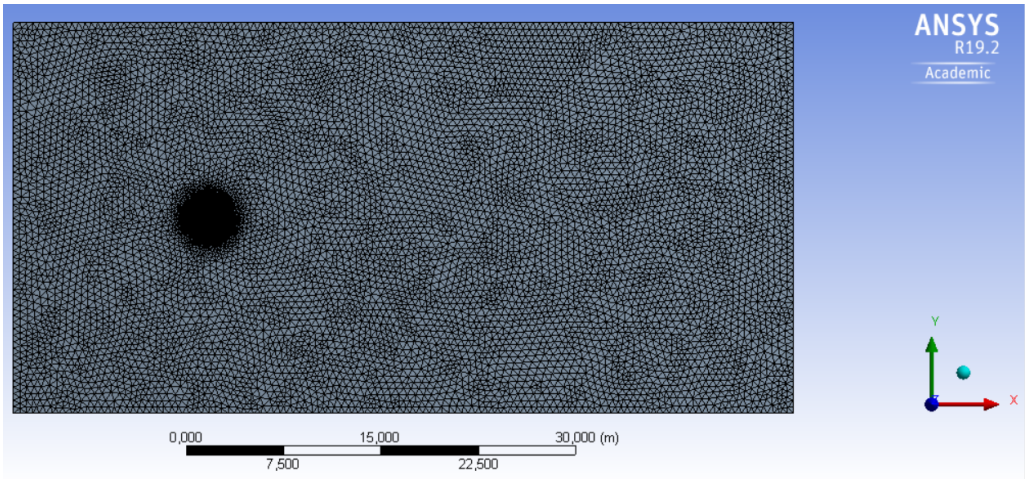

Figure 5.6 General mesh.

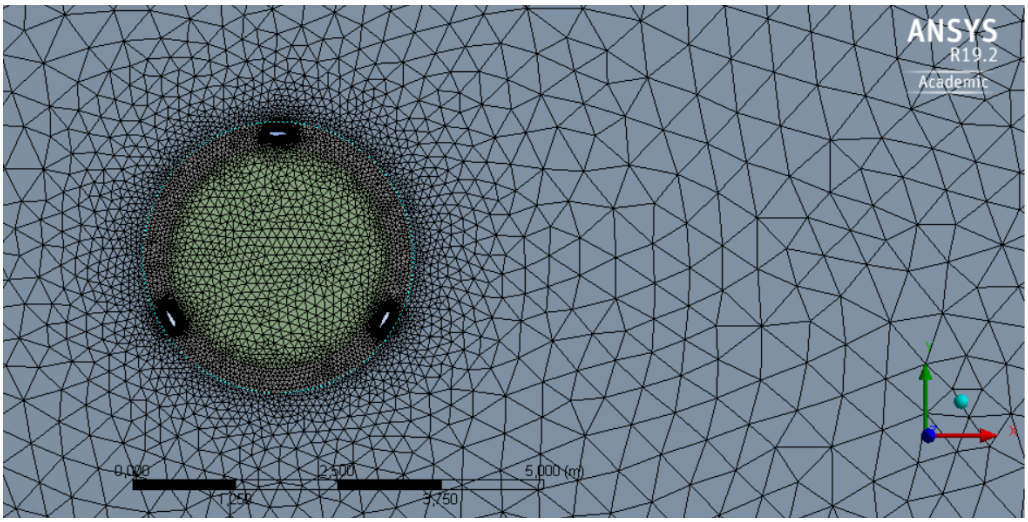

Figure 5.7 Turbine core mesh, detailed view.

Once the meshing process is finished, it is then necessary to check the quality of the results. Out of many metrics, two parameters are most influential in the successful undertaking of the simulation:

- Skewness: measures how far from the ideal (equilateral triangle or equiangular quad) each mesh element is. Thus, null skewness implies best quality, and $Skewness = 1$ implies a degenerate mesh element. [26]
- Orthogonal quality: measures the degree of alignment between the edge normal vectors and the vectors from the face centroid to the edge centroids, the value for the mesh element being the minimum of this product for all edges. Thus, $OrthogonalQuality = 1$ implies best quality (vectors completely aligned in all directions).

5.1.3 Setup and Simulation

Once the mesh has been verified, the next step is to set up the simulation. For the simulations in this study, a personal computer featuring an Intel i7-4510U processor and 16 GB RAM was used. Therefore, in order to use the full capabilities of the processor, the simulation was set up as Double Precision and using both cores.

General Setup

Due to the nature of the simulations in this study, the solver was chosen as pressure-based and transient in time.

Viscous Model

The choice of a turbulence model for a 2D VAWT simulation is still not straightforward. Early CFD simulations were undertaken using $\kappa - \varepsilon$ turbulence models, which were not sucessful in approximating flow behaviour near the wall. Thus, currently studies are prominently using $\kappa - \omega$ SST and SST Transition models [13][14]. In this study an uncalibrated Transition SST model will be used, as it enables the simulation of laminar sub-layers within the laminar flow, being a progression from the $\kappa - \omega$ SST model. Calibration of the model is out of scope for this study, as it needs extensive experimental data. Nonetheless, the uncalibrated Transation SST model proved to be sufficiently accurate for this study.

Cell Zone Conditions

In Cell Zone Conditions is where the sliding mesh concept becomes important. As such, the ”corona” region was set to have a rotating mesh motion of 13.3 rad/s (with an inlet velocity of 8 m/s amounting to $TSR = 2.5$, approximately the optimal TSR for all turbines). This motion is relative to the static mesh zone, this static mesh zone being made up of both ”exterior” and ”interior”.

Boundary Conditions

The following boundary conditions were set up in this study:

- Inlet Velocity: the wind velocity. Magnitude of 8 m/s, Turbulent Viscosity of 5% and Turbulent Viscosity Ratio of 10. These last two values are default values on ANSYS Fluent 19.2.
- Blade Rotation: for ”blade1”, ”blade2” and ”blade3”, the walls must be modelled as Moving Walls, with a rotational motion of 0 rad/s with respect to the adjacent cell zone ”corona”. This step is very important, as otherwise the blades are not modelled appropriately. The effect of this mistake can be seen on 5.3.1.

Mesh Interfaces

In this step, the Named Selections ”interface1i” and ”interface1e” are turned into ”interface1”, and ”interface2i” and ”interface2e” into ”interface2”.

Reference Values

These Reference Values are used for adimensionalisation of the variables calculated by the Fluent solver, which for this study is most important for the calculation of C_P. The Reference Values used are as per Figure 5.8.

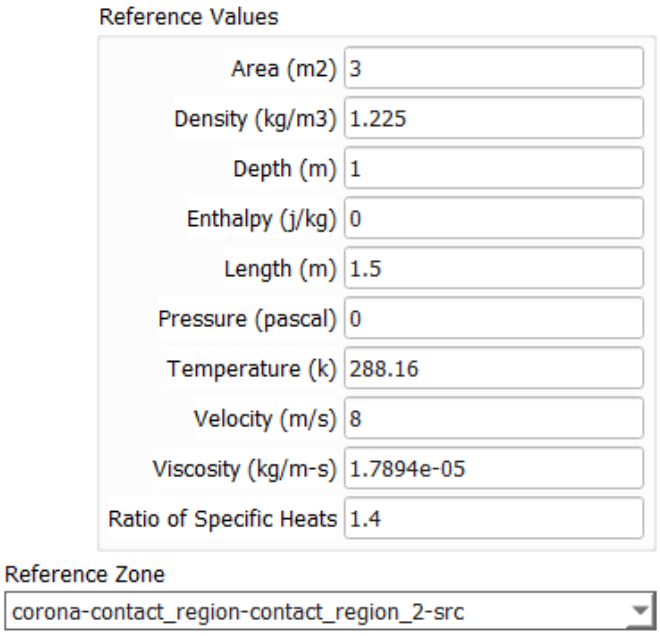

Figure 5.8 Reference Values, ANSYS Fluent.

Solution Method

The solution method used, also used by [14] is as follows:

- Scheme: SIMPLE
- Gradient: Least Squares Cell Based
- Pressure: Second Order
- Momentum: Second Order Upwind
- Turbulent Kinetic Energy: First Order Upwind
- Specific Dissipation Rate: First Order Upwind
- Intermittency: First Order Upwind
- Momentum Thickness Re: First Order Upwind
- Transient Formulation: Second Order Implicit

Monitors and Reports

As C_P is the objective variable in this study and it is directly related with the C_m as $C_P = \lambda C_m$, a monitor and a report were created for C_m, using the z-axis from (0,0,0) as moment source for ”blade1”, ”blade2” and ”blade3”.

Animations

In order to illustrate the results and also the convergence of the simulation and the different flow situations during a revolution, a velocity contour animation was created, which created one image every 5 timesteps.

Timestepping, Convergence and Solution Initialisation

As a result of [27], Rezaeiha et al. found that for convergent results, a simulation encompassing 20 turbine revolutions produced acceptable results (a 2.41% difference compared to simulating 100 turbine revolutions). Furthermore, azimuthal increments of 0.5° also provided sufficient accuracy (less than 0.5% difference compared to 0.1° per timestep). Under these premises, there thus being 720 timesteps in a revolution, each simulation took around 5 days in this study.

Convergence criteria were set as 10^{-5} and maximum 50 timesteps. A hybrid solution initialisation was undertaken.

General Parameter Summary

For further clarification, an overview of the most relevant parameters used on the simulations is show on the following Table.

Table 5.1 Key simulation parameters.

Turbine radius (R)	1.5 m
Turbine height	1m (2D study, unitary height)
Number of blades	3
Inflow velocity (V_∞)	8 m/s
Tip Speed Ratio (TSR-λ)	2.5 (approximately the optimum)
Turbulence model used	Uncalibrated Transition SST
Simulation length	20 revolutions
Azimuth discretisation	0.5°
Timestep size	$6.5 * 10^{-4}$ ms

5.2 Results: Clean Configuration

Performing a similar analysis to the one carried out on QBlade for the base configuration and both simulated passive devices, the data obtained by the moment coefficient monitor was processed on MATLAB. Figure 5.9 shows the moment coefficient over time, and Figure 5.10 the moment coefficient, averaged the whole timespan. Nonetheless, it is more representative to show the evolution of C_m over the last revolution, as the values will be nearly converged at this time range. Thi evolution, as well as the average C_m value over this last revolution, is shown in Figure 5.11.

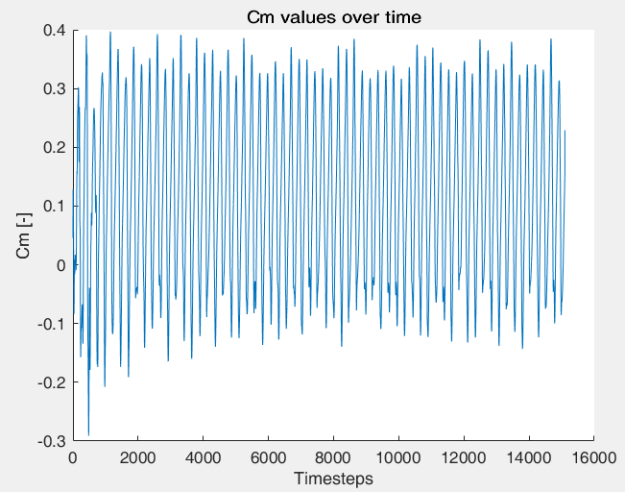

Figure 5.9 C_m over time, Clean configuration.

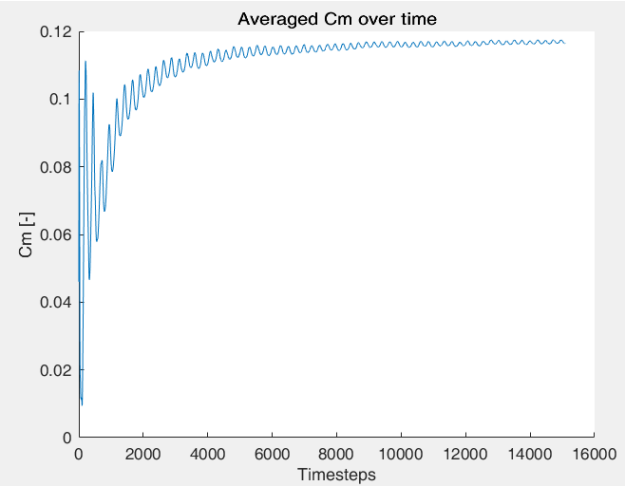

Figure 5.10 Averaged C_m over time, Clean configuration.

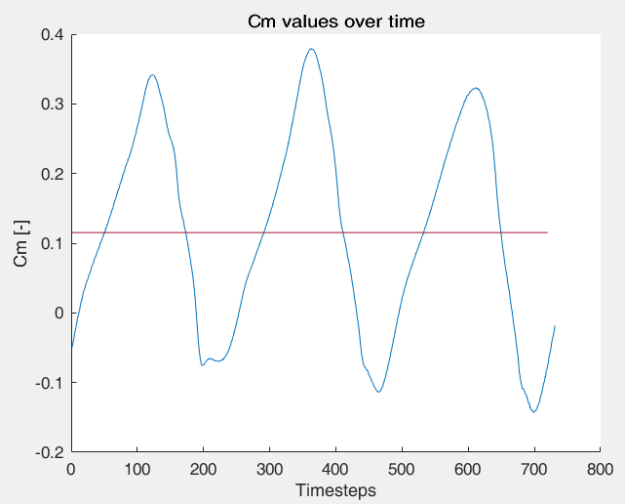

Figure 5.11 C_m over the last full revolution and average, Clean configuration.

As can be seen in Figure 5.11, the average power coefficient over the last full revolution is $C_P = \lambda C_m = 0.288$.

It is worth noting, especially upon analysis of the later two cases which will be studied, that there is no apparent regularity on blade momentum for this clean configuration. It has been observed that for this blade configuration, dynamic stall occurs in an uncontrolled, inconsistent manner in every rotation, which is the reason why the relative minima on the C_m chart are not regular. Thus, it is demonstrated why it is necessary to study and control the dynamic stall phenomenon further for a VAWT, as turbine performance is highly sensitive.

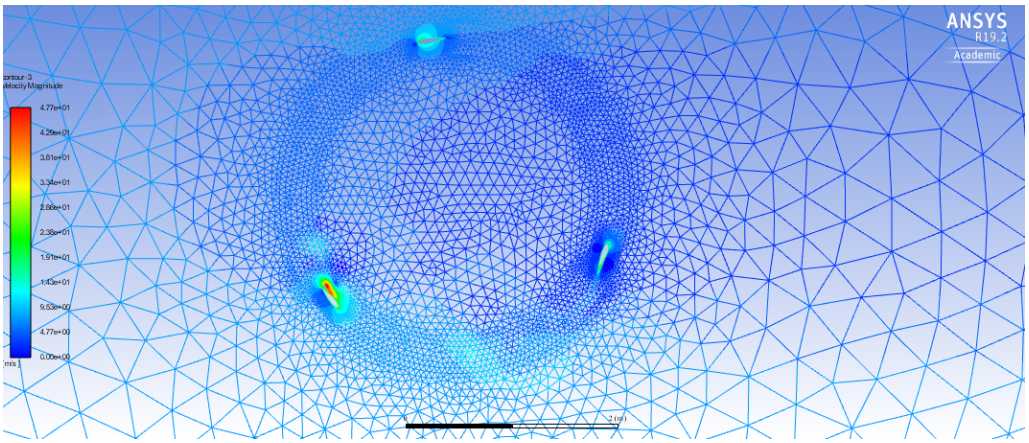

Figure 5.12 Velocity contour for a NACA0021-based turbine at its least favourable azimuth.

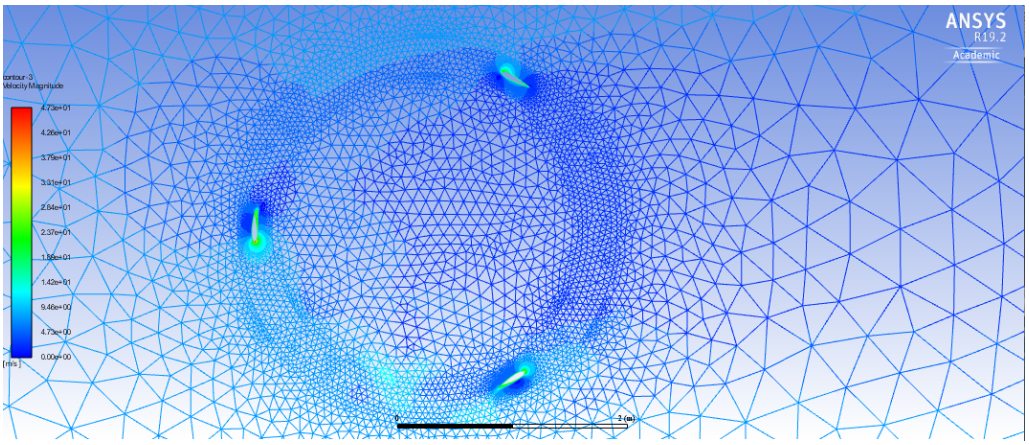

Figure 5.13 Velocity contour for a NACA0021-based turbine at its most favourable azimuth.

In order to illustrate the inconsistencies caused by dynamic stall, it is then worth including the velocity contour details for two different moments at which a blade is at its least favourable azimuth. Note the different velocity situations on Figures 5.14 and 5.15. The velocity contour at its most favourable azimuth (Figure 5.16) remains constant for all 3 blades during the permanent regime.

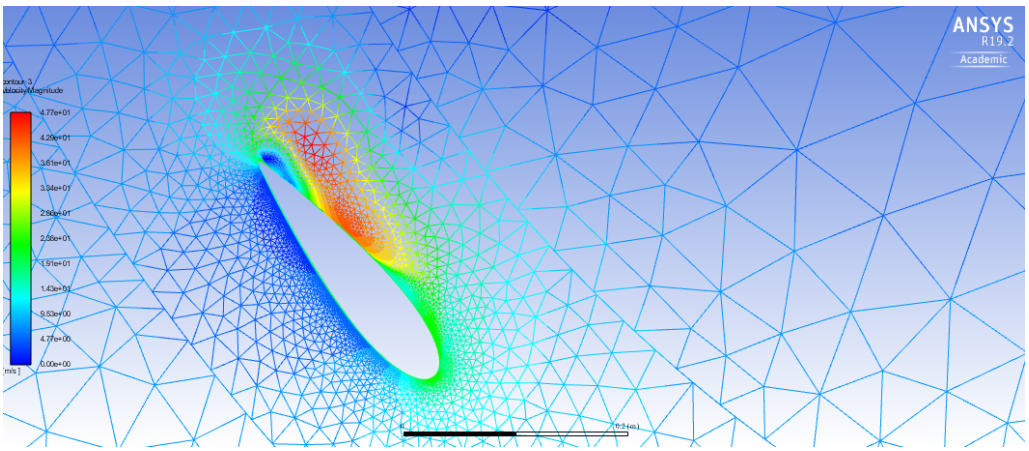

Figure 5.14 Velocity contour for a NACA0021-based turbine at its least favourable azimuth, blade detail (1).

In these two figures it is clear that the blade experiences **dynamic stall**, as the blade is stalled only for a certain azimuth range. Even though the situations illustrated by both figures are similar, maximum velocity

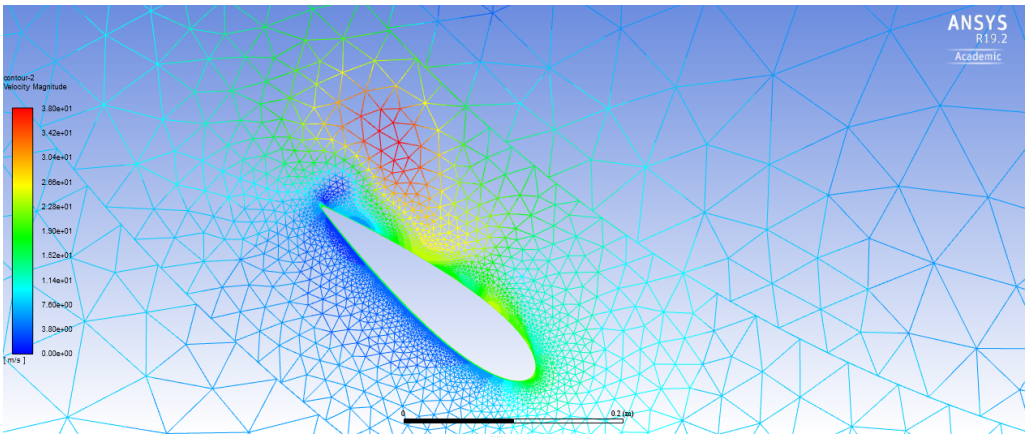

Figure 5.15 Velocity contour for a NACA0021-based turbine at its least favourable azimuth, blade detail (2).

values on the lower surface (upper surface in the picture) are lower for Situation 2. Nonetheless, vorticity seems to be higher, as the zone along the upper surface featuring low velocities (in blue) is larger.

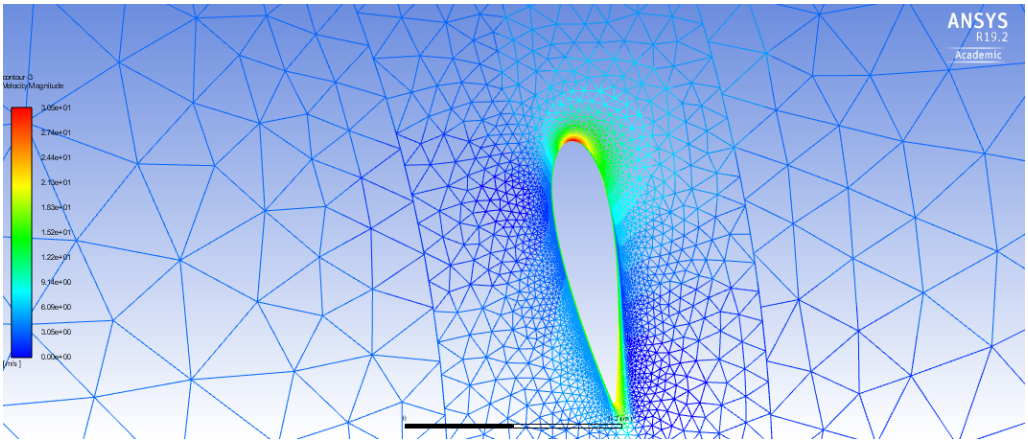

Figure 5.16 Clean configuration, most favourable azimuth, blade detail.

These most and least favourable azimuths define the position of a given blade at the moment which torque production is at its maximum and minimum, respectively. Therefore, as there are 3 blades, there will be 3 maxima and minima, these maxima and minima being defined by any blade being at one of these azimuths. The most favourable azimuth is defined by $\theta_1 = 57°$, and the least favourable azimuth by $\theta_2 = 245°$, as can be seen on Figure 5.17. These angles are constant for all 3 turbines simulated.

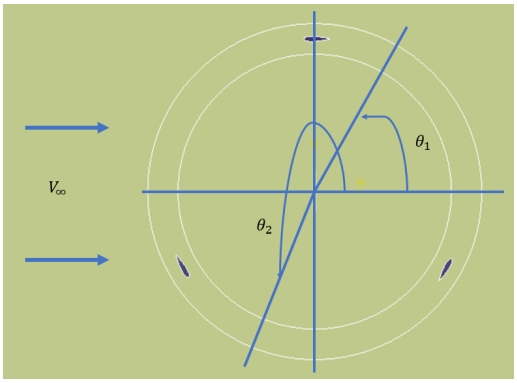

Figure 5.17 Detail on the most and least favourable azimuths.

5.3 Results: Gurney Flap Addition

It can be seen that in this case, the simulation was found to be highly stable, the end value being reached already by one third of the simulation time. The whole set of results was obtained by a second simulation, as the setup for the first simulation was incorrect and inconsistencies were found. These inconsistencies are discussed in Chapter 6. Figure 5.18 shows the moment coefficient over time, and Figure 5.19 the moment coefficient, averaged the whole timespan.

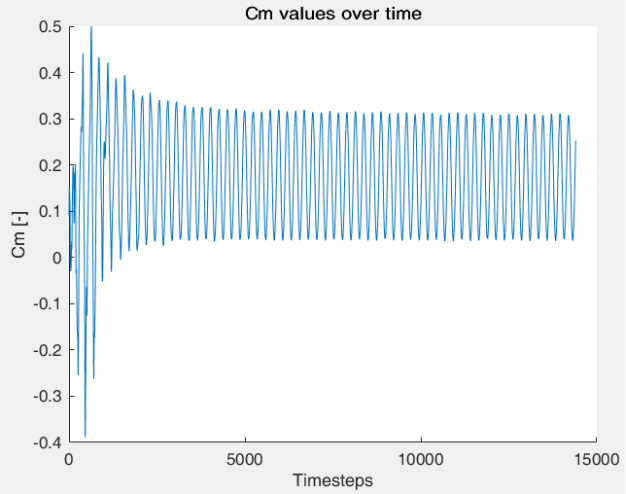

Figure 5.18 C_m over time, Gurney flap, second simulation.

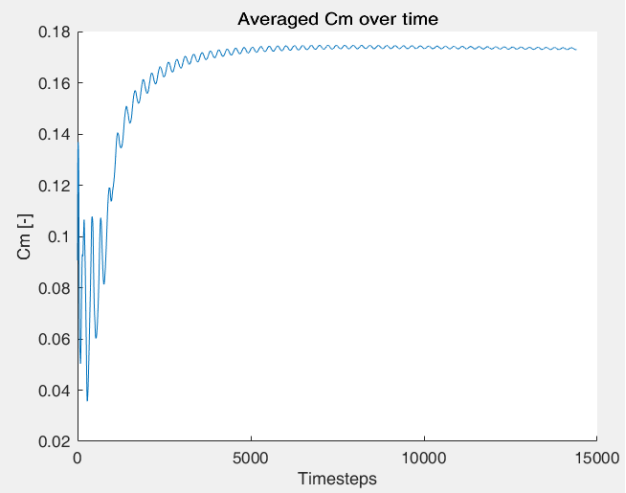

Figure 5.19 Averaged C_m over time, Gurney flap, second simulation.

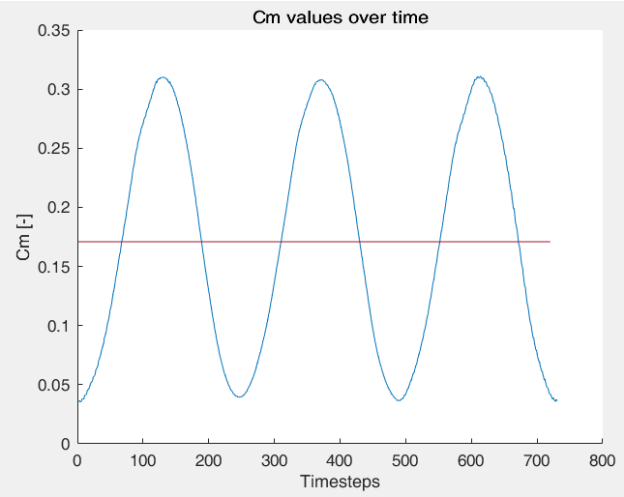

Figure 5.20 C_m over the last full revolution and average, Gurney flap, second simulation.

As can be seen on Figure 5.20, the average power coefficient over the last full revolution is $C_P = \lambda C_m = 0.427$, which is **a relative improvement of 48.26%** when compared to the clean configuration. This improvement is the highest among both airfoil modifications simulated.

It is also noteworthy how the C_m graph over the last full revolution (Figure 5.21) is by large regular, with a clear absolute maximum and minimum. This regularity of torque during a revolution could raise the possibility of simulating just a third (120°) of the turbine, for computational savings. Nonetheless, even if this simplification of the analysis would decrease computational time, it also needs to be kept in mind that this analysis is very simplified, for instance not having the rotating shaft, whose wake would also create an **asymmetry and interference in the flow**.

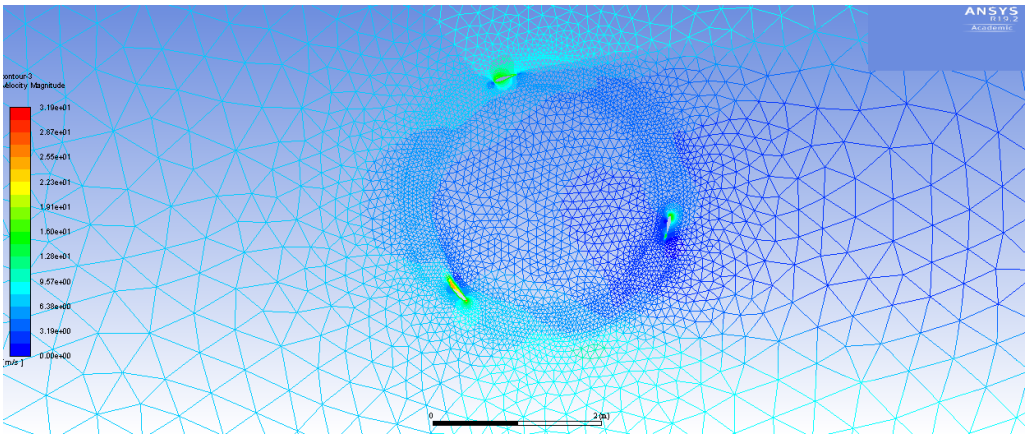

Figure 5.21 Velocity countour for the Gurney flap-equipped airfoil at its least favourable azimuth.

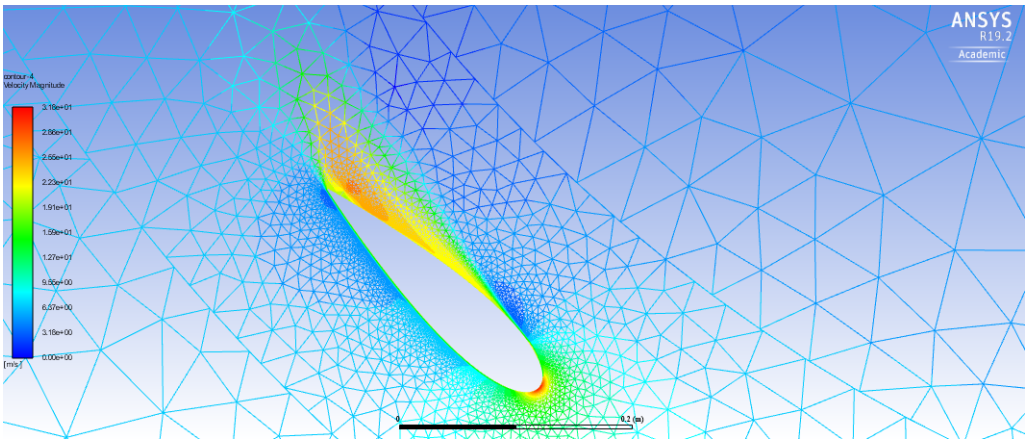

Figure 5.22 Velocity countour detail for the Gurney flap-equipped airfoil at its least favourable azimuth.

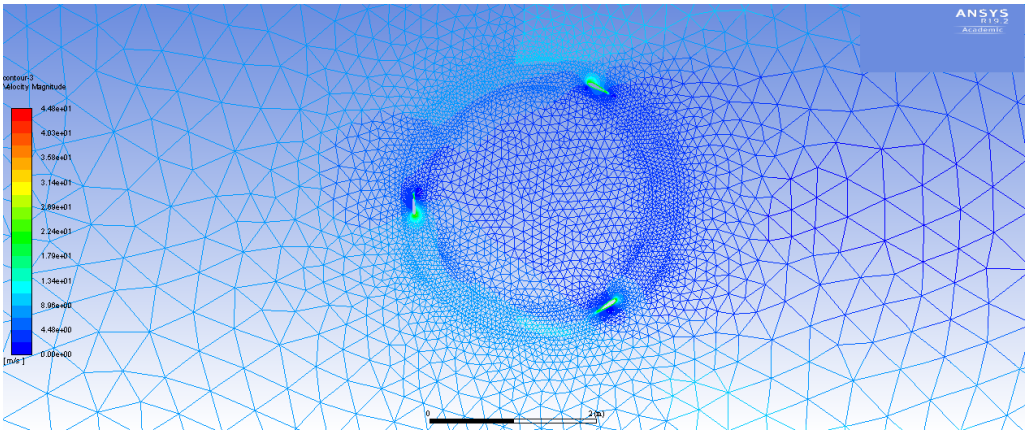

Figure 5.23 Velocity countour for the Gurney flap-equipped airfoil at its most favourable azimuth.

Upon analysis of Figure 5.22, which shows a detail of the velocity contour around the blade, it can ben seen that pressure improvements are most noticeable at the least favourable azimuths. The main reason is that flow separation areas (high velocity zones) are markedly smaller than for the clean configuration case. Due to the flow produced by the Gurney flap being more streamlined, a smaller drag component is produced.

For further detail, given that Gurney flaps have proven the most beneficial for turbine performance, Figures 5.24, 5.25, 5.26 and 5.27 show static pressure contours around the turbine, for both most and least favourable azimuths.

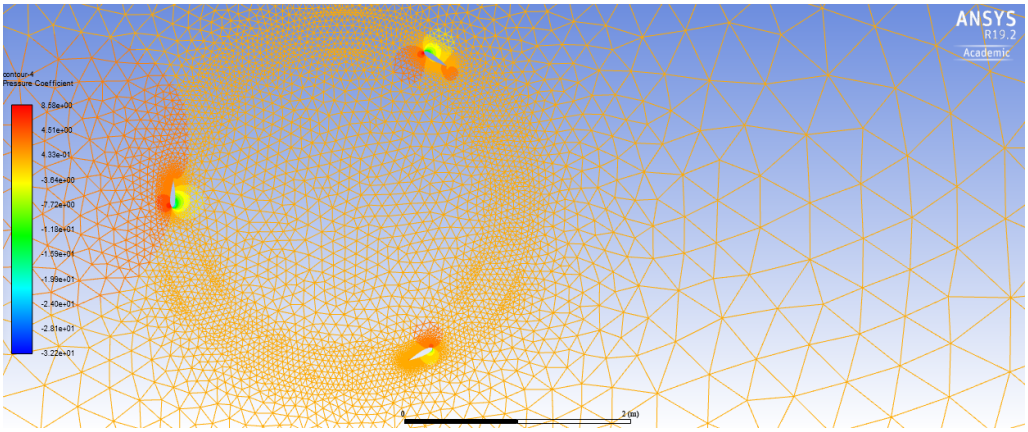

Figure 5.24 Static pressure countour for the Gurney flap-equipped airfoil at its most favourable azimuth.

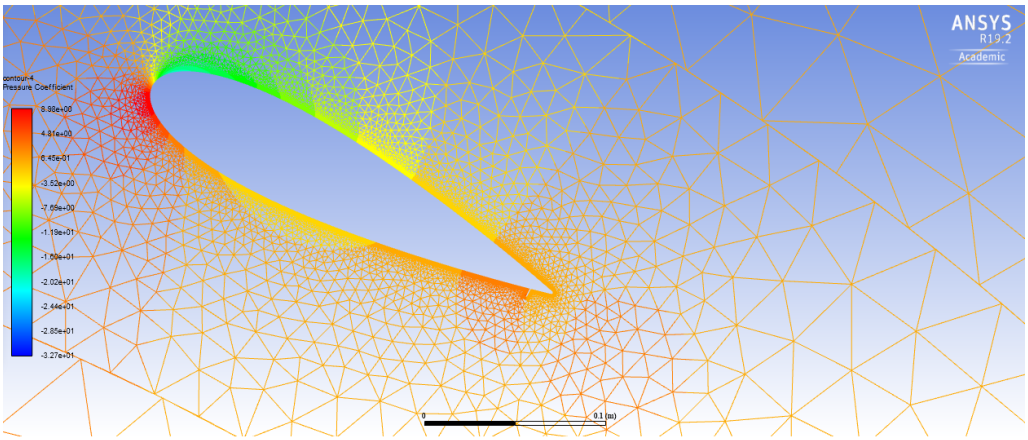

Figure 5.25 Static pressure contour detail for the Gurney flap-equipped airfoil at its most favourable azimuth.

It is seen on Figure 5.25 that at its most favourable azimuth, the blade has a typical pressure distribution for an airfoil at a small positive angle of attack, with a lower pressure side and an upper suction side.

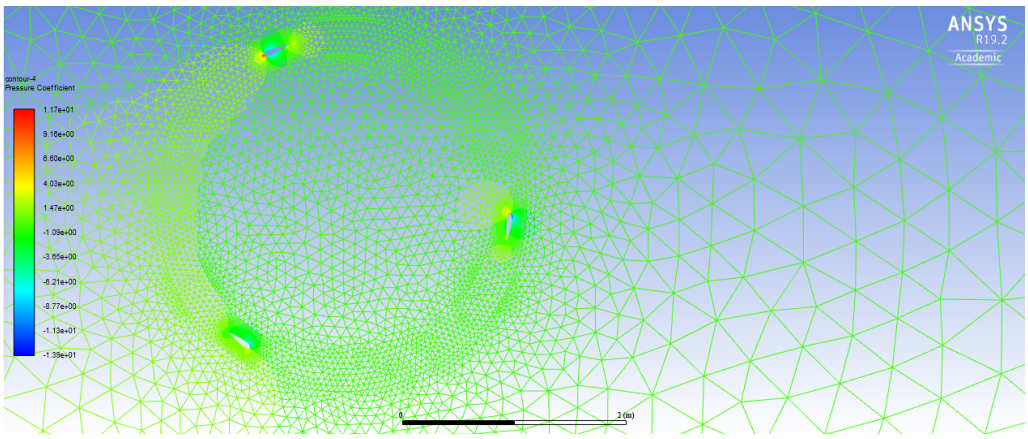

Figure 5.26 Static pressure countour for the Gurney flap-equipped airfoil at its least favourable azimuth.

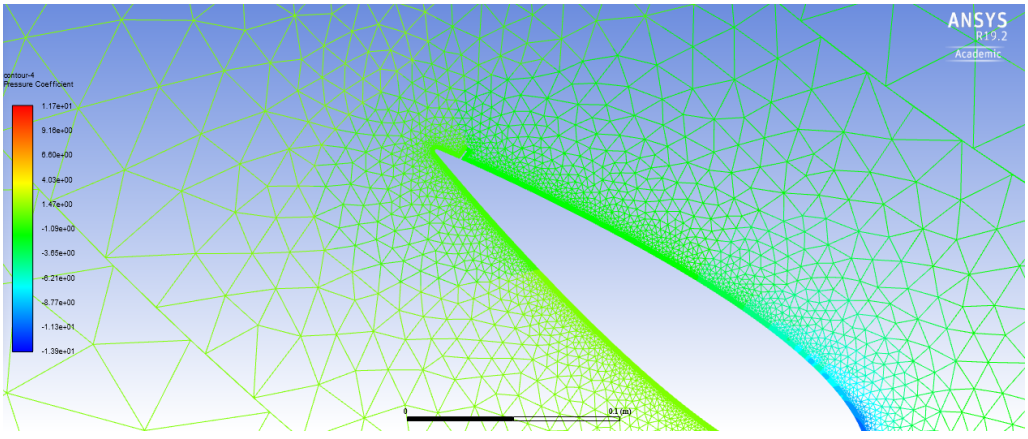

Figure 5.27 Static pressure countour detail for the Gurney flap-equipped airfoil at its least favourable azimuth.

On Figure 5.27 the situation of flow separation is very clear, as dark green and blue pressure contours are prominent on the inner side of the airfoil. This shows that there is a stalled situation on the airfoil at that least favourable azimuth.

5.4 Results: Stepped Airfoil Modification

Undertaking an analogous process to that of the two previous turbines, results were obtained for a NACA0021-based stepped airfoil. Using the same stepped airfoil also used for QBlade simulation, which was assessed as optimal by [24], no improvement over the clear configuration was found at the operational point. Figure 5.28 shows the moment coefficient over time, and Figure 5.28 the moment coefficient, averaged the whole timespan.

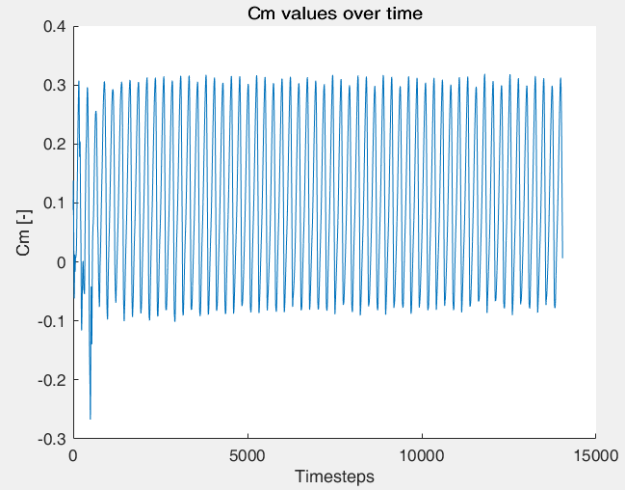

Figure 5.28 C_m over time, Stepped airfoil.

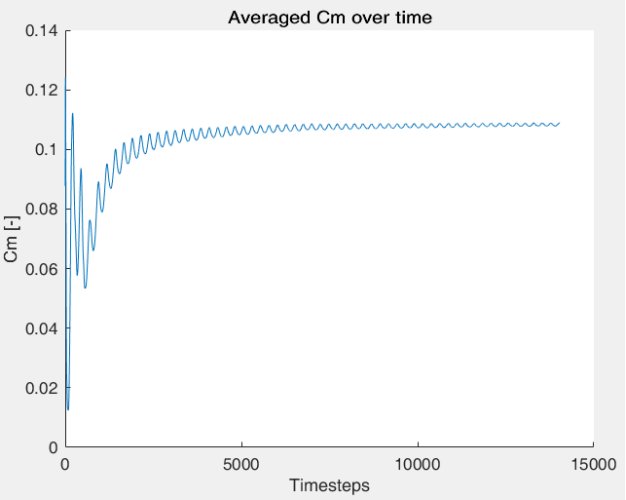

Figure 5.29 Averaged C_m over time, Stepped airfoil.

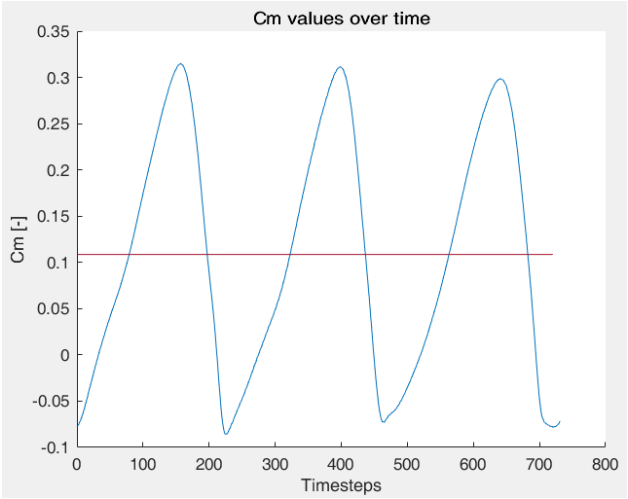

Figure 5.30 C_m over the last full revolution and average, Stepped airfoil.

As can be seen in Figure 5.30, the average power coefficient over the last full revolution is $C_P = \lambda C_m = 0.272$, which is **5.56% lower** than the clean configuration, thus representing a worsening in the operational conditions.

When compared to the clean configuration, it can be seen that there is **no apparent improvement in flow separation or stall avoidance**, which is what produces negative C_m values for the least favourable azimuth. Lower average C_m values relative to the clean configuration may also be caused because of the drag increase produced by the step at the most favourable azimuth, which reduces the amplitude between the minima and maxima in the C_m curve.

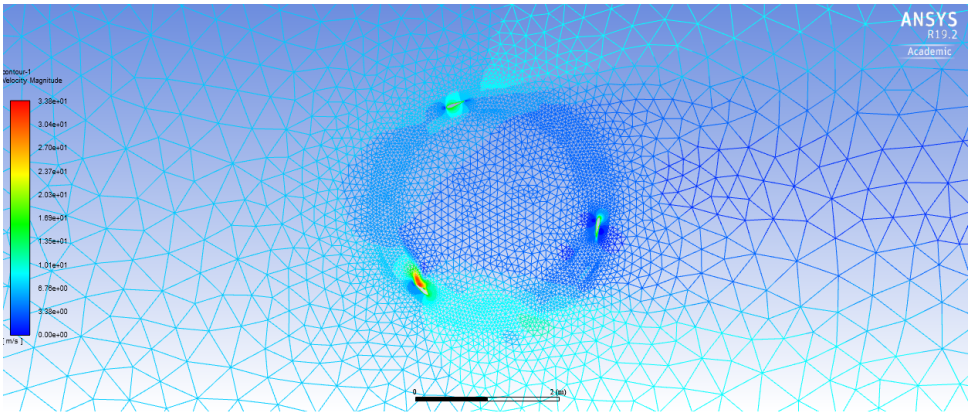

Figure 5.31 Velocity countour for the Stepped airfoil at its least favourable azimuth.

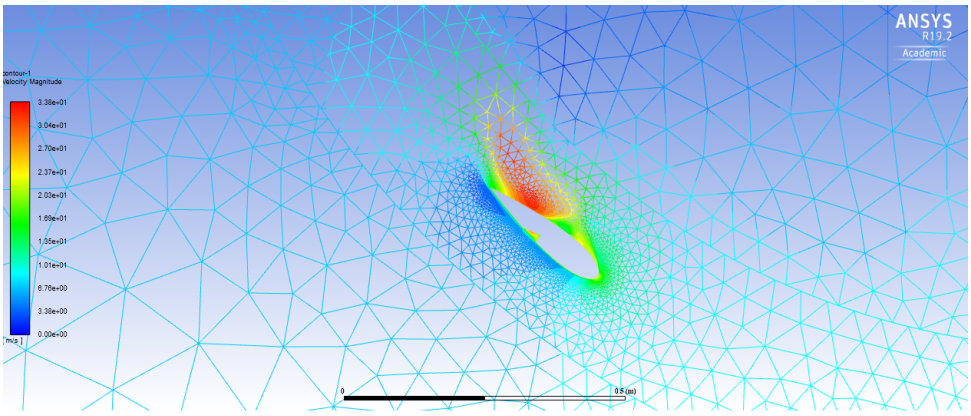

Figure 5.32 Velocity countour detail for the Stepped airfoil at its most favourable azimuth.

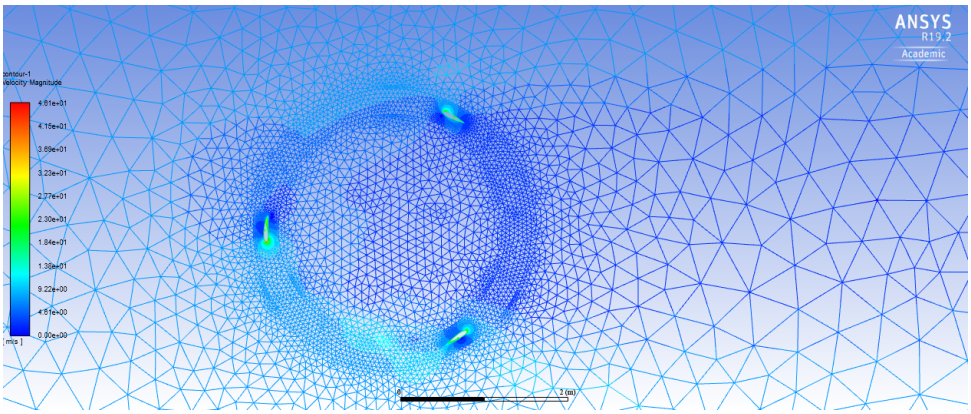

Figure 5.33 Velocity countour for the Stepped airfoil at its most favourable azimuth.

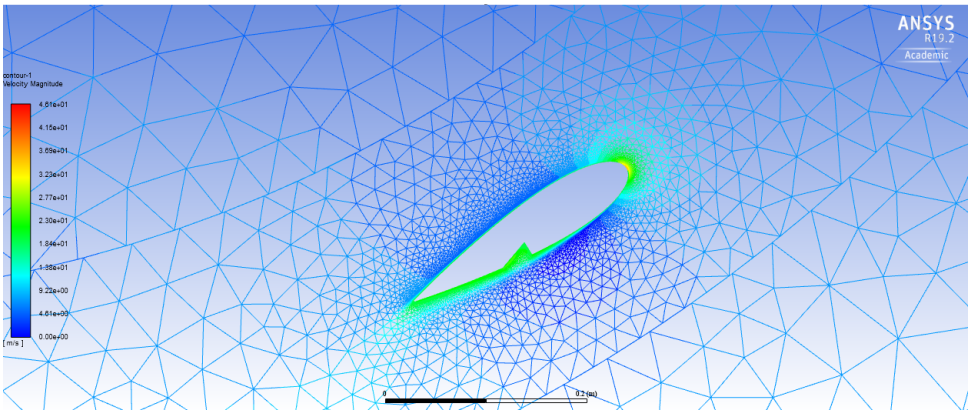

Figure 5.34 Velocity countour detail for the Stepped airfoil at its most favourable azimuth.

Upon analysis of the velocity contours 5.33 and 5.34, it can be asserted that flow separation for the least favourable azimuth is not reduced by this step configuration, when compared to the base case. Moreover, at its most favourable azimuth, the step creates some additional drag, which is why the maxima on the C_m curve over its last revolution are lower than for the clean configuration.

The test shows that a Stepped airfoil with the used placement and sizing can be asserted not to be of any benefit on the performance of the given turbine for the given operational point. Nonetheless, as was already discussed during the QBlade simulation phase, the step provides an improved performance behaviour within the low-TSR range, so such a configuration might be more beneficial for turbines where the optimal C_P is obtained for lower TSRs.

5.5 Performance Summary and Comparison with previous Studies

For clarity, a summary of the resulting performance data obtained is as follows:

Table 5.2 Performance summary.

Turbine Configuration	Power Coefficient (C_P) value	Improvement (%)
Clean configuration	0.297	Base config.
Gurney flap	0.43	44.78%
Stepped airfoil	0.28	-5.56%

In addition, for further illustration and verification, the results obtained in this project will be compared to those obtained through experimental and computational studies by other authors. As no study on the implementation of Gurney flaps and steps on the NACA 0021 airfoil is available, results on similar airfoils were investigated.

5.5.1 Clean configuration

In 2015, Dossena et al. [28] undertook extensive experimental study on a similarly sized turbine, featuring three straight blades based on a NACA 0021 airfoil. The main sizes of this turbine are as follows:

Table 5.3 Dossena et al. experimental turbine.

Turbine radius (R)	1.028 m
Turbine height (H)	1.5 m
Blade chord (c)	0.086 m
Optimal TSR	approx. 2.5

As can be seen on Table 5.3, this turbine is operationally similar to the clean configuration in this study, both because of its **sizing** and its **operational optimum** (see Figure 5.31). Dossena et al. took aerodynamic measurements 0.75D and 1.5D downstream from the turbine, and 0.75D upstream from the turbine. The results of the measurements are shown in Figure 5.31.

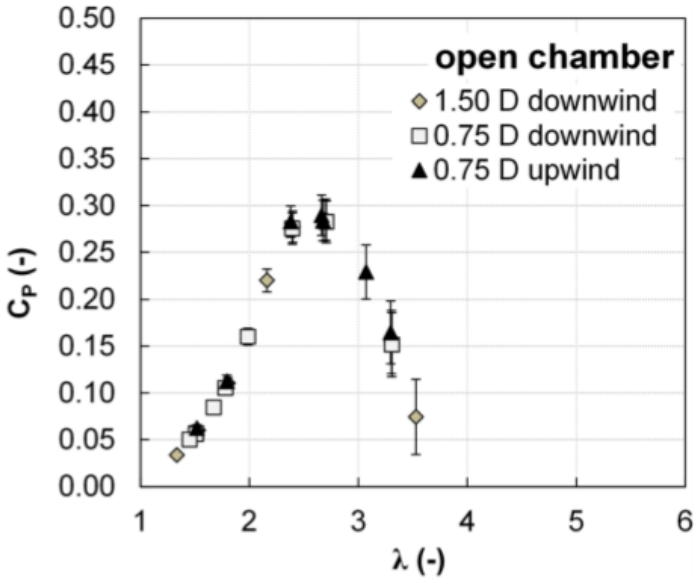

Figure 5.35 Clean configuration experimental results [28].

The optimal C_P obtained experimentally by Dossena et al. was λ=**0.28**. This is very close to the result obtained numerically in this study (**0.297**). The higher result can be attributed to it being a 2D simulation, as typical 3D effects and tower interference are not taken into consideration.

5.5.2 Gurney flap

The addition of a Gurney flap has not yet been studied extensively in a wind tunnel environment, in its application for vertical-axis wind turbines. Nonetheless, several computational results are available. One of such studies was undertaken by Ismail et al. [29], using a 1.25% chord length Gurney flap, with a dimple right before it (see Figure 5.32), applied to a NACA0015 airfoil. Ismail. et al used the dimple to reduce wake intensity, and thus reduce the drag component on the airfoil.

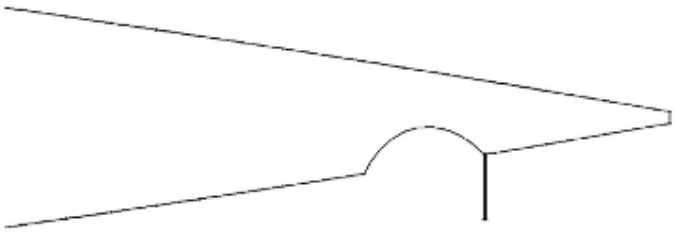

Figure 5.36 Detail of a 1.25%c Gurney flap-equipped NACA0015 airfoil with a dimple [29].

Using the $\kappa - \omega$ SST turbulent model, Ismail et al. found increases in torque relative to the clean configuration were of 35% in the steady case and **40% in the transient case**, approximately. The evolution of the tangential forces on the airfoil can be seen on Figure 5.33. Thus, this improvements found by Ismail et al. are similar to the improvements found in this project (**44.78%**).

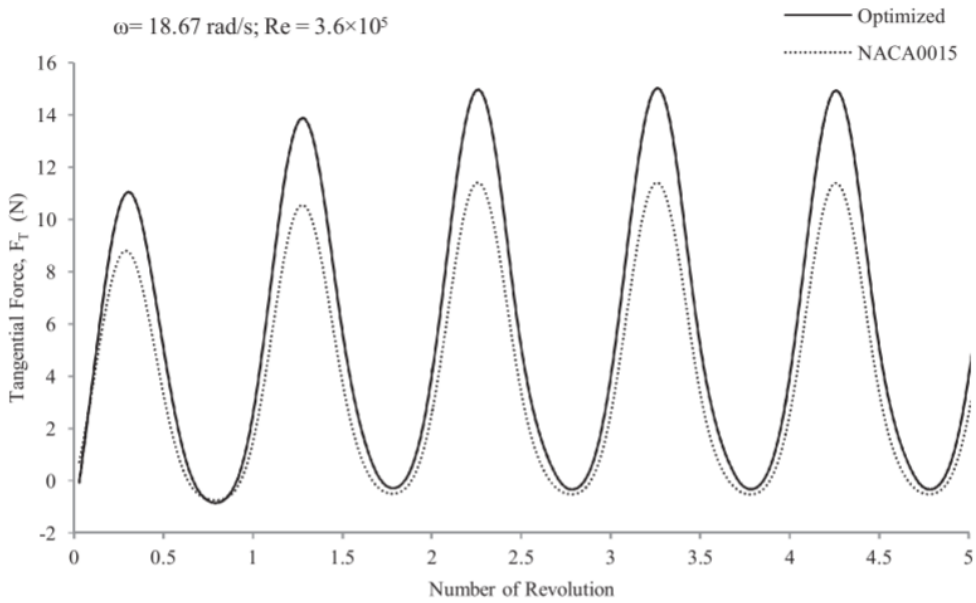

Figure 5.37 Tangential forces on a NACA0015 airfoil with a 1.25%c Gurney flap [29].

5.5.3 Stepped airfoil

For the stepped or notched airfoil, efforts have been concentrated in its self-starting capabilities, alas, improved behaviour for lower Tip Speed Ratios. Also based on a NACA0021 airfoil, Kumar et al. [30] undertook an experimental study on a notched airfoil, which had a 19%c deep, 50%c long step (see Figure 5.38). The characteristics of the general turbine tested were as follows.

Table 5.4 Kumar et al. experimental turbine.

Turbine radius (R)	0.2 m
Turbine height (H)	0.3 m
Blade chord (c)	0.1 m
Optimal TSR range	approx. 1-1.5

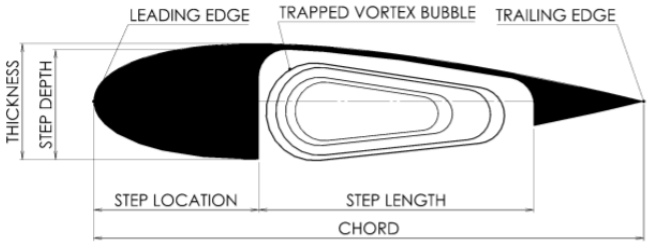

Figure 5.38 Notched airfoil, Kumar et al. experimental study [30].

The main concept behind such an airfoil is the formation of a trapped vortex bubble inside of the airfoil, for a certain azimuth range. For example, Kumar et al. found that the bubble started forming for an azimuth of 30°, and was strongest for an azimuth of 45°. This pattern would repeat every 90°.

It was found that such a configuration does improve low-TSR performance and also improves the maximum C_P, but only for low wind speeds (0-8m/s). This sensitivity to wind speed is shown on Figure 5.39. It can be seen that for higher Reynolds numbers, a notched airfoil is no longer beneficial for turbine operation.

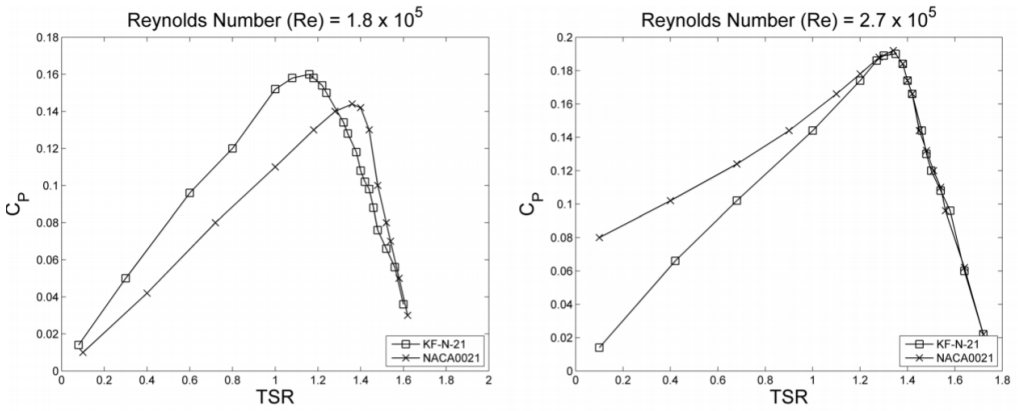

Figure 5.39 Performance variability with Reynolds number, Kumar et al. [30].

Nonetheless, this notched airfoil seems most interesting for low-cost, low-power domestic applications at sites which are not especially windy. Its design can be likened to a hybrid between a Darrieus and a Savonius turbine (due to the notch), and thus has better **startup capabilities**, as drag is more important within its operation. This importance of drag resides in the **shear layer** between the notch and the airfoil surface.

6 Inconsistencies Found During Simulation

6.1 Torque instability within the clean configuration

As has already been discussed, during the clean configuration the torque coefficient was found to be highly unstable when compared to all other simulations, and even though a general trend could be deduced, maximum and minimum values would change for every simulation.

It can be attributed to two main causes:

- Insufficient simulation time. Even though for the case studied on [27] 20 revolutions attained a stable result which did not differ significantly to simulating 100 revolutions, a longer simulation size might have been needed for the studied turbine to converge to a higher level.
- Dynamic stall control. It might be that because the clean configuration does not have any stall control device implemented, stability cannot be reached, as dynamic stall is a highly unstable process. Moreover, this has to be added to the fact that in a CFD simulation, convergence is limited. For instance, after 50 iterations in a timestep, the continuity relative error stood at 10^{-3} for the torque maxima and minima and 10^{-5} for the intermediate values.

6.2 Asymmetrical Gurney flap simulation

When the first simulation for the Gurney flap turbine was completed, it was observed that there was an asymmetry in the animation, and that one of the blades worked differently to the other two, especially when rotating past the most negative point. Later on it was detected that this was due to not setting up the Cell Zone Condition correctly for this single blade. The moving wall was set as translational instead of rotational, also relative to the ”corona” cell zone.

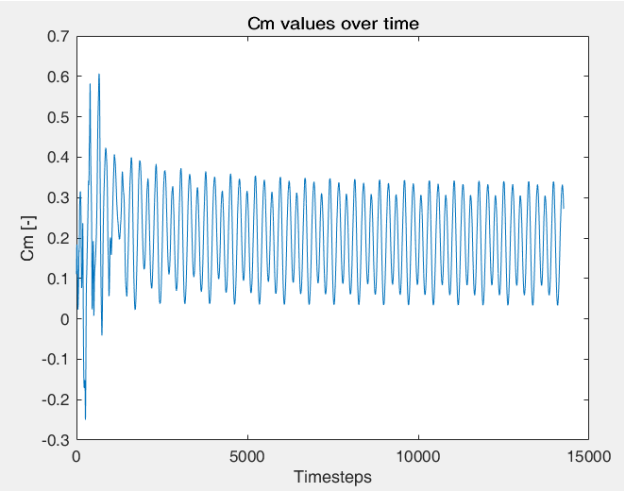

Figure 6.1 Incongruencies found during Gurney flap turbine CFD simulation, C_m over time graph.

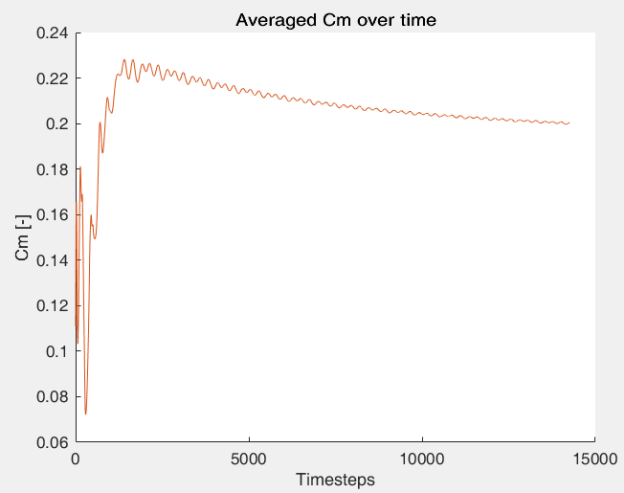

Figure 6.2 Incongruencies found during Gurney flap turbine CFD simulation, averaged C_m over time graph.

What is most noticeable about the figure below is that its best fit line would not be of the form $C(1-e^{-kt})$ like in the other cases, but it has a maximum and then its asymptote towards c (the ”final” C_m value as can be said), alas, it could be likened to $C(1-e^{-at}-e^{-bt})$. Furthermore, on Figure 6.3 it can be seen that even though all three maxima and minima should be the same or at least similar over the last revolution, there is a maximum and minimum which is different to all others. This can be attributed to the bad setup on one of the three blades, while the other two behave similarly as can be seen.

As can be seen on Figure 6.3, the average power coefficient over the last full revolution is $C_P = \lambda C_m = 0.473$, which is an improvement of 64.2% relative to the clean configuration. Nonetheless, this result is very much invalid, due to the causes which have already been discussed.

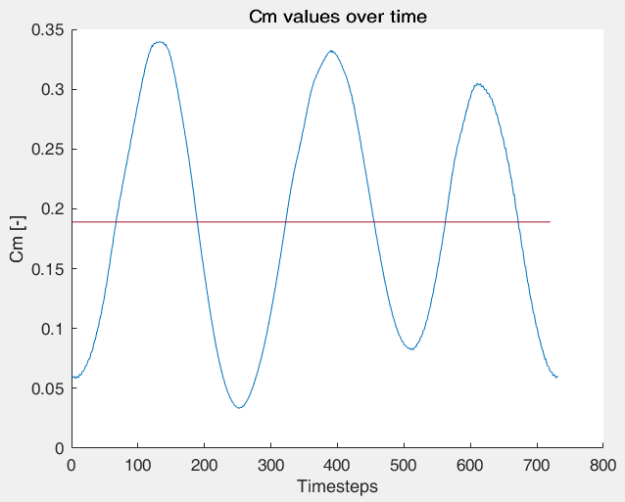

Figure 6.3 C_m over the last full revolution and average for the Gurney flap-equipped turbine.

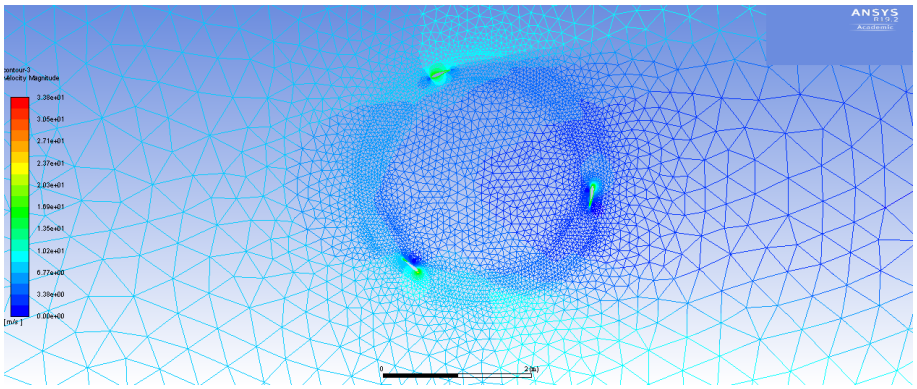

Figure 6.4 Velocity contour at the least favourable azimuth for the Gurney flap-equipped, wrongly-configured blade.

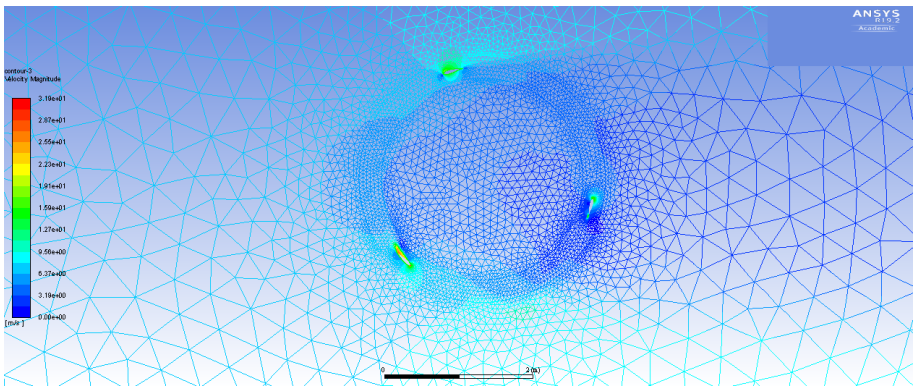

Figure 6.5 Velocity contour at the least favourable azimuth for the two remaining Gurney flap-equipped blades.

Upon analysis of Figures 6.4 and 6.6, which shows a detail on the velocity contour of the wrongly set up blade at its least favourable azimuth, it can be seen why it is not realistic, as there are no signs of flow separation, unlike it would happen for the remaining two blades. The velocity contours for the other two blades would be as per Figures 6.5 and 6.7. The situation at the most favourable azimuth would be similar for all 3 blades, see Figure 6.8.

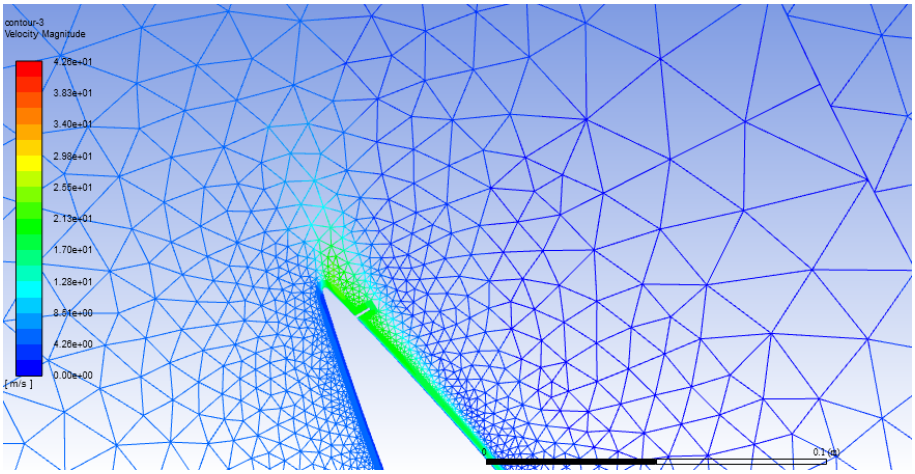

Figure 6.6 Detailed velocity contour at the least favourable azimuth for the Gurney flap-equipped, wrongly-configured blade.

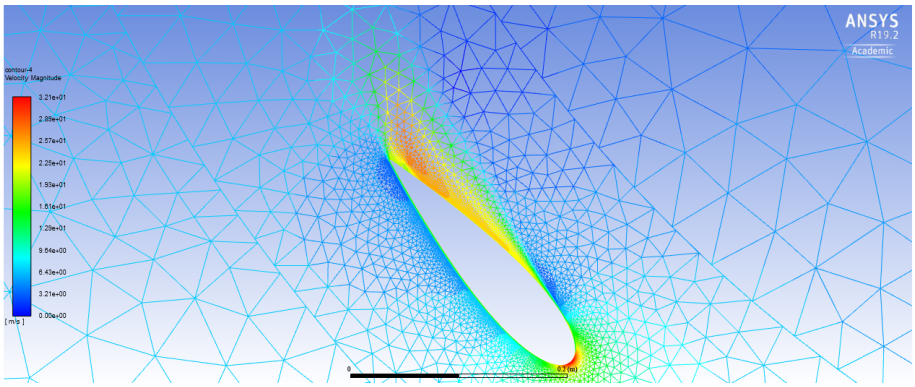

Figure 6.7 Velocity contour at the least favourable azimuth for the two remaining Gurney flap-equipped blades.

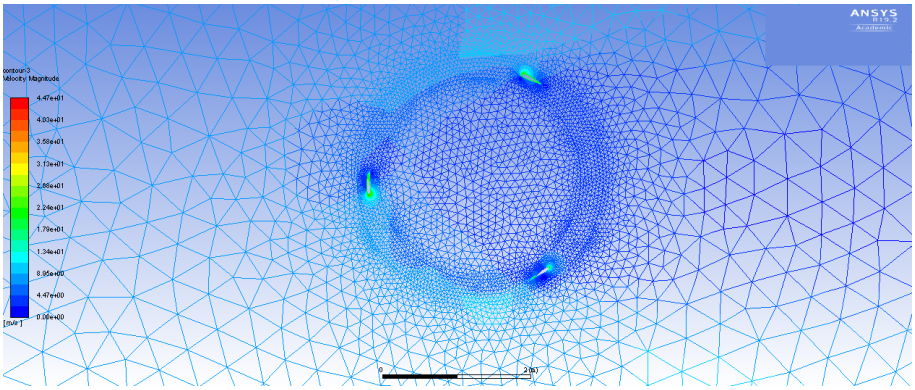

Figure 6.8 Velocity contour at the most favourable azimuth, as applicable for all Gurney-flap equipped blades.

7 Conclusion and Recommendations for Further Research

In this project, it has been verified that for a turbine based on the NACA 0021 airfoil, the effects of dynamic stall on its performance can be most significantly mitigated using Gurney flaps, improving its performance over the clean configuration by 40%. On the other hand, Liebeck's simple stepped airfoil format has proven to be highly ineffective and even negative for performance improvement.

Thus, a way forward to work on this project is to develop innovative passive devices, based on Gurney flap principles. One such concept was the implementation of a dimple on the forward side of the flap. This concept was discussed by [29], an overview of which was given in Chapter 5.5.2 of this project.

Other main points of this project have been:

- Numerical methods for airfoil polar data generation are highly unstable for non-standard geometries, and results can vary significantly between different numerical methods (see XFoil and JavaFoil).
- Using these numerically-generated polars, QBlade obtains results whose quality is uncertain. Nonetheless, even under these circumstances, QBlade can prove effective for preliminary analysis and for determining differences between different turbines and airfoils, due to its low computational costs and model complexity, when compared to DMS simulations.
- Also using numerically-generated polars, DMS obtained unrealistic results, for instance obtaining very high C_P values near the theoretical Betz's limit. DMS was only useful for a very low computational cost analysis of the optimal operational point.
- The uncalibrated Transition SST turbulent model used in this project has shown a behaviour close to experimental studies for the clean configuration. This turbulent model can therefore be verified for this configuration. Experimental studies are needed for the remaining two airfoils.

7.1 Recommendations for Further Research

The main points related to this project which need to be addressed are further model verification tasks, as well as iterative experimental design:

- An experimental wind tunnel study of the turbine, using particle image velocimetry (PIV), to obtain the torque behaviour in a steady state and verify the model.
- Calibration of the Transition SST model using experimental data, and comparison with the results of this project.
- Iterative experimental design, using the same base airfoil, and implementing different passive devices on each test, for instance changing Gurney flap placement, shape, sizing.

As there was a hiatus on VAWT research from the mid-1980s until the early 2000s, this type of turbine is still in the early development phase, and domestic applications are not yet widely available. Among others, some next steps for VAWT research are as follows:

- Further work on a low computational cost, certification-grade calculation method, which exists for HAWTs. Dynamic stall modelling proves insufficient for current VAWT calculation methods [31].
- For CFD-based computational methods, further experimental work is needed for optimal dynamic stall modelling. Many turbulent models have been used in the last decade, Transition SST proving the most reliable.
- Material research and development, for reduced manufacturing and maintenance costs.

Appendix A
Airfoil Plot Data

This appendix provides airfoil data, so as to be able to replicate the results of the study. This data can be converted into a .DAT file, which is easily imported into CATIA, SolidWorks or similar computer-aided design software, as well as into airfoil analysis suites as JavaFoil.

A.1 The NACA 0021 airfoil: clean configuration

Table A.1 NACA 0021 airfoil.

1.000000	0.002210		
0.950000	0.014120	⋮	⋮
0.900000	0.025340	0.012500	-0.033150
0.800000	0.045910	0.025000	-0.045760
0.700000	0.064120	0.050000	-0.062210
0.600000	0.079860	0.075000	-0.073500
0.500000	0.092650	0.100000	-0.081950
0.400000	0.101560	0.150000	-0.093540
0.300000	0.105040	0.200000	-0.100400
0.250000	0.103970	0.250000	-0.103970
0.200000	0.100400	0.300000	-0.105040
0.150000	0.093540	0.400000	-0.101560
0.100000	0.081950	0.500000	-0.092650
0.075000	0.073500	0.600000	-0.079860
0.050000	0.062210	0.700000	-0.064120
0.025000	0.045760	0.800000	-0.045910
0.012500	0.033150	0.900000	-0.025340
0.000000	0.000000	0.950000	-0.014120
⋮	⋮	1.000000	-0.002210

A.2 The NACA 0021 airfoil: the Gurney flap

Table A.2 NACA 0021 airfoil, Gurney flap h=0.02c, x=0.95c.

1.004630	-0.021665	⋮	⋮
1.000000	0.002210	0.012500	-0.033150
0.950000	0.014120	0.025000	-0.045760
0.900000	0.025340	0.050000	-0.062210
0.800000	0.045910	0.075000	-0.073500
0.700000	0.064120	0.100000	-0.081950
0.600000	0.079860	0.150000	-0.093540
0.500000	0.092650	0.200000	-0.100400
0.400000	0.101560	0.250000	-0.103970
0.300000	0.105040	0.300000	-0.105040
0.250000	0.103970	0.400000	-0.101560
0.200000	0.100400	0.500000	-0.092650
0.150000	0.093540	0.600000	-0.079860
0.100000	0.081950	0.700000	-0.064120
0.075000	0.073500	0.800000	-0.045910
0.050000	0.062210	0.900000	-0.025340
0.025000	0.045760	0.946000	-0.015037
0.012500	0.033150	0.946000	-0.034120
0.000000	0.000000	0.950000	-0.034120
⋮	⋮	0.950000	-0.014120
		1.000000	-0.002210

A.3 The NACA 0021 airfoil: the T-strip

Table A.3 NACA 0021 airfoil, T-strip.

1.000000	0.002210		
1.002890	0.014370	⋮	⋮
1.000460	0.014950	0.012500	-0.033150
0.997570	0.002789	0.025000	-0.045760
0.950000	0.014120	0.050000	-0.062210
0.900000	0.025340	0.075000	-0.073500
0.800000	0.045910	0.100000	-0.081950
0.700000	0.064120	0.150000	-0.093540
0.600000	0.079860	0.200000	-0.100400
0.500000	0.092650	0.250000	-0.103970
0.400000	0.101560	0.300000	-0.105040
0.300000	0.105040	0.400000	-0.101560
0.250000	0.103970	0.500000	-0.092650
0.200000	0.100400	0.600000	-0.079860
0.150000	0.093540	0.700000	-0.064120
0.100000	0.081950	0.800000	-0.045910
0.075000	0.073500	0.900000	-0.025340
0.050000	0.062210	0.950000	-0.014120
0.025000	0.045760	0.997570	-0.002789
0.012500	0.033150	1.000460	-0.014950
0.000000	0.000000	1.002890	-0.014370
⋮	⋮	1.000000	-0.002210

A.4 The NACA 0021 airfoil: the stepped airfoil

Table A.4 NACA 0021 airfoil, Stepped.

1.000000	0.002210
0.950000	0.014120
0.900000	0.025340
0.800000	0.045910
0.700000	0.064120
0.625000	0.072548
0.500000	0.035207
0.500000	0.092650
0.400000	0.101560
0.300000	0.105040
0.250000	0.103970
0.200000	0.100400
0.150000	0.093540
0.100000	0.081950
0.075000	0.073500
0.050000	0.062210
0.025000	0.045760
0.012500	0.033150
0.000000	0.000000
⋮	⋮

⋮	⋮
0.012500	-0.033150
0.025000	-0.045760
0.050000	-0.062210
0.075000	-0.073500
0.100000	-0.081950
0.150000	-0.093540
0.200000	-0.100400
0.250000	-0.103970
0.300000	-0.105040
0.400000	-0.101560
0.500000	-0.092650
0.600000	-0.079860
0.700000	-0.064120
0.800000	-0.045910
0.900000	-0.025340
0.950000	-0.014120
1.000000	-0.002210

Appendix B
MATLAB Code Compilation

This appendix provides an overview on the MATLAB code used for different parts of this study. With the addition of graph plotting, MATLAB was also used to smooth out the polars calculated by JavaFoil, which would then be used by QBlade, and to calculate the C_P and other performancevalues for the turbines, once results were obtained by ANSYS Fluent.

B.1 QBlade polar processing

Code B.1 Polar polynomial best fit.

```
clear all
clc
a=load('NACA');
x=a(:,1);
y=a(:,3);
plot(x,y,'bo')
P = polyfit(x,y,4);
xfit = -30:30;
cdfit = polyval(P,xfit);
hold on
plot(xfit,cdfit,'-')
P = polyfit(x,a(:,2),4);
xfit = -30:30;
clfit = polyval(P,xfit);

A=[xfit; clfit; cdfit]';

header1 = 'alpha';
header2 = 'Cl';
header3 = 'Cd';
fid=fopen('MyFile.txt','w');
fprintf(fid, [ header1 ' ' header2 ' ' header3 '\n']);
fprintf(fid, '%f %f %d\n', [xfit; clfit; cdfit]);
fclose(fid);true
```

B.2 ANSYS Fluent result processing

Code B.2 CFD post-processing.

```
clear all
clc
load('step.out')
data=step;
figure(1); hold on;
plot(data(:,3));
title('Cm values over time');
xlabel('Timesteps');
ylabel('Cm [-]'); hold off;

for i=1:length(data(:,3))
    mean1(i)=mean(data(1:i,3));
end

figure(2); hold on;
plot(mean1);
title('Averaged Cm over time');
xlabel('Timesteps');
ylabel('Cm [-]'); hold off;

figure(3); hold on;
plot(data(13100:13830,3));
m=mean(data(13100:13830,3));
m=m*ones(720);
plot(m);
title('Cm values over time');
xlabel('Timesteps');
ylabel('Cm [-]'); hold off;

figure(4); hold on;
plot(mean1*2.5);
title('Averaged Cm over time');
xlabel('Timesteps');
ylabel('CP [-]'); hold off;

figure(5); hold on;
plot(data(13100:13830,3));
m=mean(data(13100:13830,3))*2.5;
m=m*ones(720);
plot(m);
title('CP values over time');
xlabel('Timesteps');
ylabel('CP [-]'); hold off;
```

List of Figures

List of Tables

List of Codes

Bibliography

[1] European Wind Energy Association, ‘‘Wind energy installed capacity.’’ *http://www.windeurope.org*, 2017.

[2] Asociación Española para la Energía Eólica, ‘‘La eólica en españa.’’ *https://www.aeeolica.org/es/sobre-la-eolica/la-eolica-espana*, 2017.

[3] Agencia Andaluza de la Energía, ‘‘Energía eólica marina.’’ *https://www.agenciaandaluzadelaenergia.es*, 2016.

[4] A. Grant, C. Johnstone, and N. Kelly, ‘‘Urban wind energy conversion: The potential of ducted turbines,’’ *Renewable Energy*, vol. 33, no. 6, pp. 1157–1163, 2008. cited By 61.

[5] F. Toja-Silva, A. Colmenar-Santos, and M. Castro-Gil, ‘‘Urban wind energy exploitation systems: Behaviour under multidirectional flow conditions—opportunities and challenges,’’ *Renewable and Sustainable Energy Reviews*, vol. 24, pp. 364 – 378, 2013.

[6] P. Mehrpooya, *Improvement of Vertical-axis Wind Turbine Performance Via Turbine Coupling*. PhD thesis, Illinois Institute of Technology, 2014.

[7] M. M. A. Bhutta, N. Hayat, A. U. Farooq, Z. Ali, S. R. Jamil, and Z. Hussain, ‘‘Vertical axis wind turbine – a review of various configurations and design techniques,’’ *Renewable and Sustainable Energy Reviews*, vol. 16, no. 4, pp. 1926 – 1939, 2012.

[8] I. O. N. PARASCHIVOIU, ‘‘Double-multiple streamtube model for studying vertical-axis wind turbines,’’ *Journal of Propulsion and Power*, vol. 4, pp. 370–377, Nov. 2018.

[9] P. Tchakoua, R. Wamkeue, M. Ouhrouche, T. A. Tameghe, and G. Ekemb, ‘‘A new approach for modeling darrieus-type vertical axis wind turbine rotors using electrical equivalent circuit analogy: Basis of theoretical formulations and model development,’’ *Energies*, vol. 8, no. 10, pp. 10684–10717, 2015.

[10] Wikipedia, ‘‘Airfoil lift and drag.’’ *https://upload.wikimedia.org/wikipedia/commons/a/a2/Airfoil_lift_and_drag.jpg*.

[11] D. Marten, G. Pechlivanoglou, C. N. Nayeri, and C. O. Paschereit, ‘‘Nonlinear lifting line theory applied to vertical axis wind turbines: Development of a practical design tool,’’ *Journal of Fluids Engineering*, vol. 140, no. 2, p. 021107, 2018.

[12] D. Marten, A. Bianchini, G. Pechlivanoglou, F. Balduzzi, C. N. Nayeri, G. Ferrara, C. O. Paschereit, and L. Ferrari, ‘‘Effects of airfoil’s polar data in the stall region on the estimation of darrieus wind turbine performance,’’ *Journal of Engineering for Gas Turbines and Power*, vol. 139, no. 2, p. 022606, 2017.

[13] M. Kortleven, ‘‘Simulation verication and optimization of a vertical axis wind turbine using cfd,’’ Master’s thesis, TU Delft, 2016.

[14] R. Lanzafame, S. Mauro, and M. Messina, ''2d cfd modeling of h-darrieus wind turbines using a transition turbulence model,'' *Energy Procedia*, vol. 45, pp. 131 – 140, 2014. ATI 2013 - 68th Conference of the Italian Thermal Machines Engineering Association.

[15] ANSYS, ''Introductory fluent notes.'' *https://www.southampton.ac.uk/~nwb/lectures/GoodPracticeCFD/Articles/Turbulence_Notes_Fluent-v6.3.06.pdf* , 2006.

[16] E. A. Bah, L. Sankar, and J. Jagoda, ''Investigation on the use of multi-element airfoils for improving vertical axis wind turbine performance.,'' No. 0 in Aerospace Sciences Meetings, American Institute of Aeronautics and Astronautics, Nov. 2018.

[17] E. Nieuwenhuizen and M. Köhl, ''Differences in noise regulations for wind turbines in four european countries,'' in *Proceedings: Euronoise*, pp. 333–338, 2015.

[18] O. Eboibi, L. A. M. Danao, and R. J. Howell, ''Experimental investigation of the influence of solidity on the performance and flow field aerodynamics of vertical axis wind turbines at low reynolds numbers,'' *Renewable Energy*, vol. 92, pp. 474 – 483, 2016.

[19] A. J. Fiedler and S. Tullis, ''Blade offset and pitch effects on a high solidity vertical axis wind turbine,'' *Wind engineering*, vol. 33, no. 3, pp. 237–246, 2009.

[20] JavaFoil, ''The boundary layer method.'' *http://www.mh-aerotools.de/airfoils/javafoil.htm*.

[21] D. Marten, *QBlade v0.95 Guidelines for Lifting Line Free Vortex Wake Simulations*, 06 2016.

[22] C. S. Jang, J. C. Ross, and R. M. Cummings, ''Numerical investigation of an airfoil with a gurney flap,'' *Aircraft Design*, vol. 1, no. 2, pp. 75 – 88, 1998.

[23] I. Malael, R. Bogateanu, and H. Dumitrescu, ''Theoretical performances of double gurney flap equipped the vawts,'' *INCAS Bulletin*, vol. 4, no. 4, p. 93, 2012.

[24] F. Finaish and S. Witherspoon, ''Aerodynamic performance of an airfoil with step-induced vortex for lift augmentation,'' *Journal of Aerospace Engineering*, vol. 11, no. 1, pp. 9–16, 1998.

[25] F. Frunzulica, A. Dumitrache, and B. Suatean, ''Numerical investigations of passive flow control elements for vertical axis wind turbine,'' in *AIP Conference Proceedings*, vol. 1637, pp. 331–340, AIP, 2014.

[26] SAS, ''Ansys help.'' *https://www.sharcnet.ca/Software/Ansys/16.2.3/en-us/help/*, 2015.

[27] A. Rezaeiha, I. Kalkman, and B. Blocken, ''Cfd simulation of a vertical axis wind turbine operating at a moderate tip speed ratio: Guidelines for minimum domain size and azimuthal increment,'' *Renewable Energy*, vol. 107, pp. 373 – 385, 2017.

[28] V. Dossena, G. Persico, B. Paradiso, L. Battisti, S. Dell'Anna, A. Brighenti, and E. Benini, ''An experimental study of the aerodynamics and performance of a vertical axis wind turbine in a confined and unconfined environment,'' *Journal of Energy Resources Technology*, vol. 137, no. 5, p. 051207, 2015.

[29] M. F. Ismail and K. Vijayaraghavan, ''The effects of aerofoil profile modification on a vertical axis wind turbine performance,'' *Energy*, vol. 80, pp. 20–31, 2015.

[30] P. M. Kumar, M. M. R. Surya, R. Kethala, and N. Srikanth, ''Experimental investigation of the performance of darrieus wind turbine with trapped vortex airfoil,'' in *2017 3rd International Conference on Power Generation Systems and Renewable Energy Technologies (PGSRET)*, pp. 130–135, IEEE, 2017.

[31] C. Galinos, ''Study of design load cases for multi-megawatt onshore vertical axis wind turbines,'' 2015.